LUND
UNIVERSITY

MASTER THESIS

Active stabilisation of a micro-sized fibre cavity using tilt locking to enable quantum operations on single ions

Author:
Jannek Jonas HANSEN

Supervisor:
Andreas WALTHER

A thesis submitted in fulfillment of the requirements
for the degree of Master of Science
project duration 8 month

in the

Quantum Information Group
Atomic Physics

Submitted May, 2021

LUND UNIVERSITY

Abstract

Active stabilisation of a micro-sized fibre cavity using tilt locking to enable quantum operations on single ions

by Jannek Jonas HANSEN

In this thesis, the tilt locking scheme is applied to create an error signal that monitors length changes in a fibre-based microcavity. To find a robust and precise locking technique is an essential step towards quantum operations on single rare-earth ions doped in microcrystals as proposed in [1]. Quantum computing and information is a frontier of modern physics. Many scholars believe that Quantum technology will have a significant impact on future computation and communication [2]. It holds the potential to not only enable a whole new area of science by simulating highly relevant complex quantum systems like molecular structures but also to create the possibility of computer encryption for which safety is guaranteed by the laws of nature. The most recent publications demonstrating functioning quantum computers have shown that quantum computations are already in the realm of state of the art technology [3, 4]. However, there are currently multiple approaches to building quantum computers. At the moment, there is no clear picture of which approach for quantum operation is going to be the most applicable. The quantum information group at Lund University focuses on rare-earth-ions doped into crystals to be used as qubits [5]. The long-lived energy levels of these ions can be used for quantum computations. It is necessary to make use of the Purcell effect to enable the interaction with single ions. This effect describes the emission probability for a photon by an atom in an optical resonator [6]. The reduction of the volume leads to an enhanced emission probability and therefore enables single ion readouts. By placing the substrate in an optical microcavity with a length of just a few micrometres, the phase volume is reduced. These planoconcave cavities consist of a coated concave fibre-tip on one side and a highly reflective mirror on the other [7].
The main limitation towards single ion readout is mechanical vibration which induces changes in the cavity length. There are well-known ways to actively stabilise the length of cavities, such as the Pound–Drever–Hall stabilisation, side-of-fringe locking, or the so-called tilt locking [8, 9]. In this work, the different locking techniques are compared and tested for their applicability to stabilise fibre-based microcavity. In a short cavity, the resonant peaks are very far apart such that we can only use the resonant frequency, which is also used for the ion manipulations because the next resonance is no longer in the high reflectivity range of the coating. To avoid interfering with the main experiment, we base our locking scheme on the higher-order transverse modes of the cavity. These higher orders naturally occur in the cavity due to the asymmetric shape. This work derives the coupling coefficients of an incoming Gaussian beam into the higher-order transverse modes of the cavity to study the resulting error signal. The wavelength of the light which excites the higher orders does not disturb the fundamental quantum operations because the higher-order modes are resonant on a slightly shorter wavelength than the main resonance due to the Gouy-shift. Furthermore, a test setup to show the functionality of the tilt locking scheme for the microcavity was built and tested. In this thesis, I theoretically and experimentally demonstrate the tilt locking error signal of a microcavity.

LUND UNIVERSITY

Popular science description

Active stabilisation of a micro-sized fibre cavity using tilt locking to enable quantum operations on single ions

by Jannek Jonas HANSEN

Quantum mechanics is one of the most well-established theories in modern physics. But in our day to day life, we barely observe any quantum effects. This is because quantum states need to be kept isolated from the environment to stay in a quantum state. To uncouple the quantum states from the environment is one of the main challenges that need to be overcome when building a quantum computer. In Lund, we want to build a quantum computer prototype that uses ions in crystals as quantum states. With laser light, we can interact with the single ions and measure their internal state. But single ions can always only emit and absorb a single photon. To make it more likely for the ions to interact with the light, we put them into a cavity. A cavity, in this case, is two mirrors in between which the light bounces back and forth.

When a peak of the light wave in the cavity perfectly lines up with the peak of the wave from the previous round-trip, so-called constructive interference occurs. This means the light could bounce up to thousands of times before escaping the cavity. This leads to a large enhancement of the emission from the ions. For the peaks from all round-trips to line up perfectly, however, the distance between the mirrors has to be exactly an integer number of wavelengths and very stable.

The biggest problem we face at the moment is that these mirrors are vibrating, which disturbs the perfect line-up, and reduces the emission enhancement. There are tricks on using the light that bounces back and forth in the cavity to detect these vibrations. When we make the laser light enter the cavity with a slight angle, the light takes a different path inside the cavity compared to the light without an angle. This different path means that the vibrations of the mirrors affect them differently. We place a detector behind the cavity to detect the two light beams. In this signal, we can see the vibration of mirrors and correct them. Several techniques to do this are well known and have been very successfully used, for example, to detect gravitational waves. The difficulty for the cavity we use in Lund is that we have to work with an extremely short cavity to interact with the single ions. The distance between the two mirrors in our setup is less than the thickness of a human hair. This short length makes it difficult to find a suitable scheme to measure the vibration in our cavity.

In this work, we find a method of using a tilted incoming beam to measure the vibrations sufficiently well. This technique, known as tilt locking, promises to enable the interaction with single ions in the next-generation experiment.

Acknowledgements

I want to express my appreciation to the Quantum information group at Lunds University. My special thanks to Mohammed Alqedra, who supported me on all levels of my Master thesis, from the introduction to experimental work with optics over theoretical discussions about the higher orders cavities to the art of buying the right things on *THORLABS*.
I am also incredibly thankful for the discussions with Lars Rippe. He motivated me by showing genuine interest in the theoretical background work I was doing in the beginning of the thesis. Lars was always open to answer all my questions about electric circuits and detector as well as the shot-noise limit.
Haitham El-Ella, unfortunately, left Lund after half of the time I had for my thesis, but until then, he was a great help in finding the best locking scheme. Over lunch, he was able to teach me everything about tilt locking I needed to know to understand its potential.
My colleagues Abdullah Abdelatief and Safi Rafie-Zinedine helped me a great deal in the lab to set up the fibre cavity.
I wish to express my special gratitude to my supervisor, Andreas Walther, who offered me to do this thesis under his supervision and supported me along the way. Additionally, I would like to thank Frances Hill and Dougal Elias for their support regarding the English languish.

Special thanks to my girlfriend and family, who gave me emotional support in the difficult times when the Covid-19 situation forbade me to work on campus and valuable direct interactions with my fellow researchers.

Contents

List of Figures

List of Tables

List of Abbreviations

FWHM	**F**ull **W**idth **H**alf **M**aximum
$\Delta\nu$	Free spectral range
$\delta\nu$	Spectral width
$\mathcal{F}$	Finesse
NIR	**N**ear **I**nfra **R**ed
µm	micrometer
nm	nanometer
PDH locking	**P**ound **D**rever **H**all locking
$\mathbf{Y_2SiO_5}$	Yttrium Orthosilicate
Eu	**Eu**ropium
Pr	**Pr**aseodymium
Nd	**N**eo**d**ymium

Chapter 1

Introduction to single ion detection using a stabilized micro-cavity

The Quantum information group at Lund's University wants to demonstrate a flexible microcavity setup. This microcavity should be able to be tuned to interact with different single rare-earth ions in nano-crystals. Currently, the main limitations are mechanical vibrations. One way to overcome these vibrations is to install a dedicated locking scheme that corrects length changes in the cavity. In this thesis, the theory describing microcavities is summarized and extended. The theory lays the foundation to understand, simulate and compare different locking schemes in chapter 3. The experimental work of this thesis is done by implementing the tilt locking approach, which is the most promising following the calculations. The setup to test the functionality of tilt locking was built from scratch.

Cavity locking is commonly used to lock the frequency and phase of laser light to a stable cavity [8]. In this work, these techniques are applied in reverse to lock the length of the cavity to the frequency or power of a laser source. This has been, on a very different length scale, famously used to detect gravitational waves [10]. The difficulties discussed and solved in this work result from the short cavity length of just a few µm and the fact that the locking scheme should not affect or interfere with the main single ion readout.

1.1 Quantum Computing

In the history of modern physics, there has been an immense output of applications that are so deeply involved in our day-to-day life that it is hard to imagine living without them. The most common examples include the laser, telecommunication, or the modern camera, to mention a few. But the one which arguably has the most significant impact on contemporary society is the computer in its various forms.

The use of quantum computers promises to have a significant impact on future research and our understanding of the world [2]. Quantum supremacy has been shown by a group from Google in 2018 [3] and very recently by the group around Han-Sen Zhong in China, who built a quantum–computer based on photonics [4] in contrast to the US group whose computer is based on superconducting circuits using the concept of Josephson junctions for their qubits.

A quantum computer that can approach real-world problems better than a classical computer needs to consist of a sufficient number of qubits with a low error. On the one hand, quantum mechanics is why this type of computer is in some cases more efficient and has significant advantages over a classical computer, especially when simulating quantum systems like molecules or semiconductor structures. On the other hand, this is also why difficulties occur when realising such a device. The

physics of quantum mechanics is sensitive to measuring the state of the system. This is such that measuring the system projects the state of the system to one measurement base, which means that the information in the other bases is lost. This behaviour is called collapsing the quantum state; thus, the system is fragile to noise in any form which couples the system to the environment. How long the physical setup can keep the qubits isolated from the environment determines the lifetime and coherence time of the qubit. The lifetime of the qubit could be, for example, the lifetime of the energy state in a trapped ion. At the same time, the coherence time is the time taken until the ion is out of phase with the laser pulse, which initiated the energy transition [11, 12].

In 2000, DiVincenzo introduced his "five plus two requirements" for a working quantum computer [13]. The first and currently the most critical requirement is to have a "scalable physical system with well-characterised qubits". In order to build a qualified quantum computer, the number of qubits must be scaled up compared to the current working systems [5]. There are currently multiple approaches to a functioning quantum computer. Until now, most attention went to superconducting circuit-based systems as described in [14]. On the other hand, there has been much research on cold trapped ions for quantum computing, which has shown high fidelity quantum gates [15, 16]. It is not yet clear which physical realisation of a quantum computer will most efficiently upscale the number of high fidelity qubits.

The quantum information group in Lund is following the approach of designing a quantum computer based on rare-earth-ion-doped crystals, which promise great scalability once functioning on a single ion readout scheme [5]. The current limitation which prevents the system from interacting with single ions in the crystal is mechanical vibration. In order to suppress these vibrations, current work focuses on a new mechanical setup holding the microcavity in which the crystal sits. Even with this new setup, the implementation of active stabilisation of the cavity length is required to meet the stability conditions. This active feedback loop to lock the length will be based on so-called tilt locking. In this thesis, a tilt locking error signal is demonstrated on a microcavity.

1.2 Cavity enhanced single ion computation

Ions doped into a crystal can be viewed as naturally trapped ions. The crystal structure holds the ions in place with much higher trap potential compared to artificial ions traps. For comparison, the typical distance between two ions in an artificial trap is on the order of µm, while the distance of the doped ions in the crystal is in the order of nm.

In order to use this advantage of doped crystals, the crystal needs to be cooled down below 4 K to suppress decoherence through phonon interaction. Long living energy states with an optical transition can be used as qubits. Rare-earth elements doped in Y_2SiO_5 crystals have an inner-shell dipole transition in the 4f shell which has a long lifetime. Inner shell transitions are forbidden in the free atom but become weakly allowed when doped into a crystal. Another advantage of transitions in the 4f shell is its long coherence time due to the fully populated 5s and 5p shells, which are spatially further away from the core of the atom and act as a Faraday cage [11, 1]. The typical radial structure of rare-earth atoms is shown in figure 1.1

The idea of rare-earth-ion-doped crystal-based quantum computing is based on long-living optical accessible energy states of the doped ions as qubits. It has already

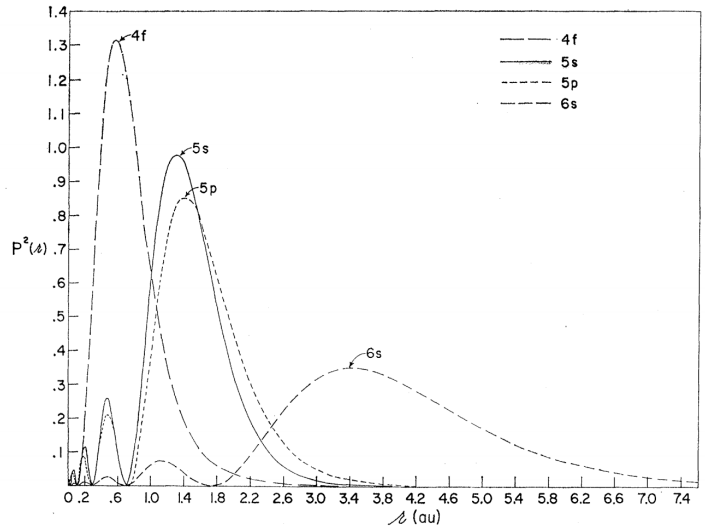

FIGURE 1.1: In this plot, the radial distributions of the outer shells of Gadolinium are shown. The 4f shell is spatially closer to the core than the 5s and 5p shells. The distribution of the shell structure can be generalised for all rare-earth atoms. This figure is reprinted from [17].

been shown that a functioning qubit can be created out of an ensemble of ions [1]. When scanning the crystals with a broad frequency around the transition frequency of the 4f transition, it is revealed that the transition frequency is broad. This broadening results from the random position in the crystal structure as every ion is trapped in a slightly different potential, this mean that the resonance frequency of the dipole transition is shifted. The width of these frequencies is called the inhomogeneous linewidth of the crystal, typically in the order of 5 to 50 GHz. The homogeneous linewidth of the single ions is in the order of kHz as conceptually demonstrated in figure 1.2 [11][18].

Using this effect, one can separate different qubits in frequency. These ensembles consist of millions of ions, which is an advantage when using these for quantum memory. When doing quantum computations, the dephasing between the ions is a limitation for the coherence time of this qubit system. A truly scalable quantum computer based on rare-earth doped crystals has to be designed to interact with single ions in the crystal [18].

1.2.1 Single ion readout

To interact with single rare-earth ions in a crystal is challenging because of the low fluorescence of a single ion by itself. Despite the difficulties, interactions with single rare-earth ions in crystals have already been shown [19, 20]. The advantage of a fibre-based microcavity is to have a very open system. The same microcavity can target different ions by tuning the length to the resonance of that ion. In order to have a larger sample, the microcavity is also tunable in the transverse axis and can thereby target several nanocrystals on the mirror surface.

The long lifetime which is so desirable for quantum computing makes it harder to read these states out due to low fluorescence. In an effort to overcome this problem, two different types of rare-earth ions get doped into the crystal. One has a long

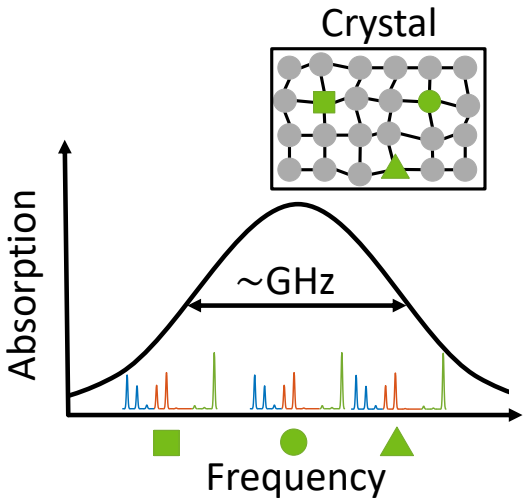

FIGURE 1.2: The inhomogeneous linewidth is in the order of GHz. Thereby it is many orders of magnitudes broader than the homogeneous linewidth of the ions, which is in the order of kHz. The frequency of the dipole transition depends on the environment in the crystal. This figure is reprinted from [11].

lifetime (e.g. Eu) acting as a qubit, and another ion (e.g. Nd or Pr) has a high capacity for enhancement, functioning as the readout ion [5, 1].

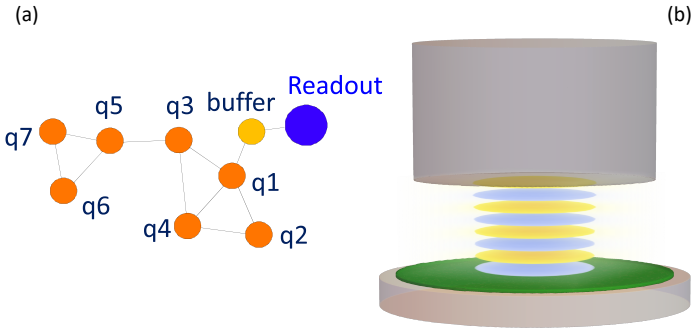

FIGURE 1.3: In figure (a), the concept of a readout scheme is illustrated. One readout ion interacts with up to 100 qubit ions. Figure (b) indicates the idea that the substrate containing the nanocrystals is coated onto the flat mirror forming the cavity. Here, the fibre is coming from above. When the light is resonant in the cavity, it forms a standing wave, as indicated here by colour coding the phase of the light. This Gaussian beam has its waist at the surface of the flat mirror onto which the nanocrystals are coated. The figure (a) is reprinted from [5].

The long-living qubit-ions surround the readout-ions with shorter living excited states as conceptually demonstrated in figure 1.3. A laser beam with the right wavelength can be tuned to communicate with readout-ions in different positions of the

crystal. This makes use of the fact that the energy transition frequencies depend on the ions position and its surrounding in the crystal.

The crystal is placed in a microcavity to enhance the photon's probability of interacting with the ions. This cavity enhancement is based on the Purcell–effect. This effect describes the enhanced fluorescence in a small mode volume with a high finesse [21, 11]. This quantum mechanical effect enhances the spontaneous emission of photons which are resonant in the mode-volume. Without this enhancement, it would not be possible to detect the feedback from the single readout-ions in the crystal.

In order to fit the rare-earth ions into the microcavity, they are doped into nanocrystals. These nanocrystals are coated onto one of the mirrors of a microcavity as illustrated in figure 1.3. The length of this cavity is tuned to be resonant with the energy transition of the readout-ions. With a focus on maximising the Purcell–enhancement, the cavity needs to have a high finesse.

High finesse in a cavity translates into a narrow resonance peak; thus, when the length of the cavity drifts off, the resonance with the readout frequency is lost. In this thesis, options for monitoring cavity length changes producing an error signal are theoretically discussed. For microcavities, tilt locking is a promising approach to lock the cavity length with high precision. In chapter 3 the experimental setup to demonstrate the error signal from tilt locking is reviewed. The properties of this error signal are discussed in chapter 4. To build an active feedback loop that reacts to the error signal correcting the length changes is the next logical step and is discussed in chapter 5.

1.3 Overview of the thesis

In chapter 2 I give a summary of the theory needed to understand the physical properties of the resonant light inside the microcavity. The theoretical results in chapter 2.3 are an overview of the calculations I performed in detail in appendix A. These calculations are my own worked, and I did them without help except for the cited papers. I compared the different locking schemes side-of-fringe locking, Pound-Drever-Hall (PDH) locking, and tilt locking in chapter 3. The locking schemes are well known and understood techniques; my contributions were simulating them for our system's properties and comparing them in this respect. In order to distinguish the best option for the microcavity, I simulated the expected error signal for the three options. By discussing the result of the simulations and the technical installation of locking schemes, I conclude that tilt locking is the most suited for this particular experiment.

To demonstrate the error signal experimentally, I put a proof of principle experiment together, measuring the tilt locking error signal. Chapter 4 gives an overview of the experimental setup. My colleagues manufactured the fibre tip itself but I independently designed and built the optical setup and the electrical connection to the detector. I calculated the behaviour of the beam waist after the cavity to order a fitting aspheric lens. In chapter 5 I discuss the error signal by combining the results of the simulations and the experimental outcome. In chapter 6 I summarize the few missing steps and required tools to lock the main experimental setup containing rare-earth ions.

Chapter 2

Theoretical discussion

The stability of the phase and frequency of the interacting light is crucial when performing quantum operations on single ions in a nanocrystal. Length changes of the microcavity induce phase changes in the resonant light. Therefore the length stability of the cavity is one of the main limitations in single-ion detection. In order to lock the cavity to the required length, different locking techniques are compared, namely side-of-fringe locking, Pound-Drever-Hall stabilisation, and tilt locking. These techniques are used to lock the cavity length to the frequency or the power of a laser [8, 22]. In this chapter, an overview of the theory required to understand the different locking schemes is presented.

2.1 Physics of the cavity

The simplest example of an optical cavity would be two mirrors facing each other, such that a photon would bounce back and forth between them. For the light to build up a standing wave inside an optical resonator, the effective distance between these two mirrors has to be an integer multiple of half the wavelength of the resonating light. More generally speaking, the resonance condition is that the phase of the light needs to be preserved after each round trip. A cavity can be described by its length and the reflectivity of the mirrors. Knowing these properties, one can calculate the finesse, which is a measure for the average number of round trips the light is doing inside the cavity before it gets transmitted through one of the mirrors or is lost by other means. In the following chapters, the focus will be on the plano-concave cavity because that is the one formed between the fibre-tip and the highly reflective mirror in the microcavity setup [7]. A fibre-base microcavity is conceptually visualised in figure 2.1.

One characteristic measure of a cavity is its free spectral range:

$$\Delta\nu = \frac{c}{2L} \tag{2.1}$$

here L is the effective cavity length and c is the speed of light. The free spectral range is the distance between the resonance peaks of the cavity in frequency space as shown in figure 2.2. The width of these resonance peaks is characterised by the spectral width $\delta\nu$.

$$\delta\nu = \frac{\Delta\nu}{\mathcal{F}} \tag{2.2}$$

Here $\mathcal{F}$ is the finesse. The finesse can be calculated with the reflectivity of the mirrors.

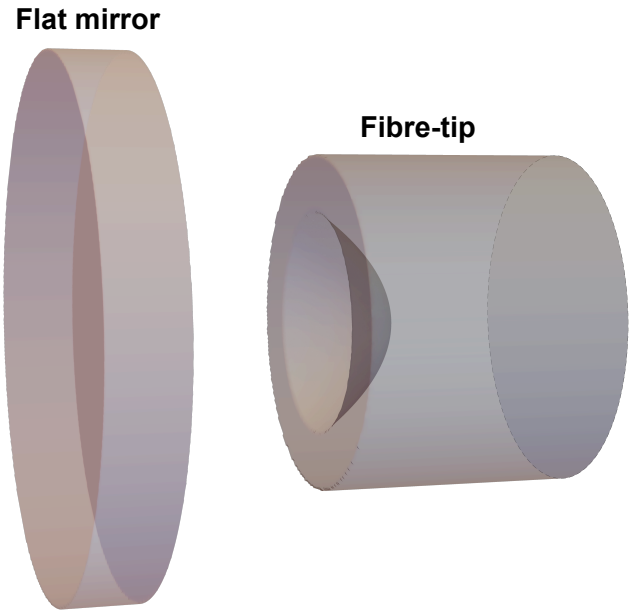

FIGURE 2.1: The coated fibre-tip and the flat mirror create a plano-concave cavity.

$$\mathcal{F} = \frac{\sqrt{r_1 r_2}}{1 - r_1 r_2} \tag{2.3}$$

$r_{1,2}$ are the field reflectivities of the two mirrors. If they are the same, the finesse can also be written in terms of the power reflectivity R, which is experimentally easier to determine.

$$\mathcal{F} = \frac{\sqrt{R}}{1 - R} \tag{2.4}$$

The shape of the resonance peaks shown in figure 2.2 have a Lorentzian shape:

$$I(\nu) = \frac{I_{max}}{1 + (2\mathcal{F}/\pi)^2 \sin^2(\pi\nu/\nu_F)} \tag{2.5}$$

as described in detail in [23]. Equation 2.5 is the function representing the power intensity of the light transmitted through the cavity, where I_{max} is the maximal intensity given by the incoming light at that frequency. $\nu_F = \frac{c}{2L}$ is the lowest frequency that resonates inside the cavity.

From the formulae 2.1 and 2.2, one can see that the free spectral range, as well as the spectral width of microcavities defined by their short length (of just a few μ-meters), are very broad because of the $1/L$ dependency.

2.2 Characterising the cavity in the fibre-tip

The physical dimensions of the cavity distinguish the properties of the resonant modes inside the cavity. The resonance condition in a cavity is that the phase of

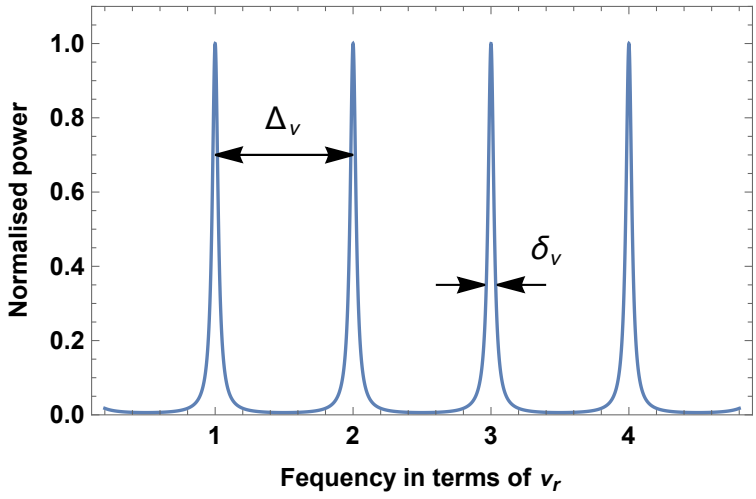

FIGURE 2.2: The free spectral range $\Delta\nu$ is the distance of two resonance peaks in frequency space while the spectral width $\delta\nu$ is a measure for the width of the peak. This plot is reproduced from [23].

the resonant light has to be an integer multiple of 2π after one round-trip. The total accumulated phase after travelling two times the length of the cavity can therefore be expressed as:

$$\exp\left[-ik2L + i\xi_n(2L)\right] = \exp\left[-i2\pi q\right] \tag{2.6}$$

$$\Rightarrow 2Lc\frac{2\pi}{\lambda} - c\xi_n(2L) = 2\pi qc \tag{2.7}$$

$$\nu_{res} = \frac{c}{\lambda} = \frac{cq}{2L} + c\frac{\xi_n(2L)}{4L\pi} \tag{2.8}$$

where $\xi(2L)$ is the additional phase shift known as the Gouy shift, explained below. The index $_n$ indicates that the additional phase might vary for different allowed solutions.

The concept of wave optics gives an accurate approximation when describing the standing waves inside a cavity. From there, it can be derived that the Gaussian beam is a solution to the paraxial Helmholtz equation. The Helmholtz equation governs the way light expands. In a general form the Hermite–Gaussian mode function can be written as:

$$u_n(x,z) = \left(\frac{2}{\pi}\right)^{(1/4)} \left(\frac{\exp\left[i(n+1)\xi(z)\right]}{2^n n! w(z)}\right)^{1/2} H_n\left(\frac{x\sqrt{2}}{w(z)}\right) \exp\left[-i(kz + \frac{kx^2}{2R(z)}) - \frac{x^2}{w^2(z)}\right] \tag{2.9}$$

The derivation can be found in detail in [23]. To generalise the solution to three dimensions, the third dimension can be added by multiplication:

$$u_{nm}(x,y,z) = u_n(x,z)u_m(y,z) \tag{2.10}$$

The equation consists of:

$$w(z) = w_0\sqrt{1+\left(\frac{z}{z_0}\right)^2} \tag{2.11}$$

which is the behavior of the beam radius depending on the beam-waist w_0 at $z = 0$. This is the waist of the beam-spot at the focal point. The beam-waist of the Gaussian beam has a flat wave-front; therefore, the radius of curvature at this point is infinity. In general, the radius of curvature of a Gaussian beam can be written as:

$$R(z) = z\left(1+\left(\frac{z_0}{z}\right)^2\right) \tag{2.12}$$

Where z_0 is the so-called Rayleigh length, which is the distance from z=0 to the point where the beam radius has grown to $w(z_0) = \sqrt{2}w_0$. The Rayleigh length can then be calculated.

$$z_0 = \frac{\pi w_0^2}{\lambda} \tag{2.13}$$

Higher-order modes are multiplied with the Hermite polynomial $H_n(\frac{x\sqrt{2}}{w(z)})$ of the same order. The Hermite polynomials are an orthogonal set of functions with respect to the weight function e^{-x^2} [24].
The additional phase $\xi(z)$ in the Hermite-Gaussian beam is known as the Gouy shift.

$$\xi(z) = \arctan\left[\frac{z}{z_0}\right] \tag{2.14}$$

This shift can be explained by considering the transverse momentum of the Gaussian beam [25]. The higher orders experience a bigger Gouy shift because they are spatially wider. Due to this shift, higher orders with the same frequency are resonant at a different length according to the resonance condition in equation 2.8. In the figure 2.3 the zeroth-order, generally referred to as the Gaussian beam, is visualised inside a cavity with dimensions similar to those expected in the microcavity.
In microcavities, higher-order Hermite–Gaussian modes can be observed. To understand at which frequencies they resonate, equation 2.8 and equation 2.9 are compared. The comparison reveals that the additional phase is the the Gouy shift and the dependency on the index $_n$ is defined by the order.

$$\nu_{res} = q\frac{c}{2L} + (n+1)\frac{c}{2L}\frac{\xi(2L)}{2\pi} \tag{2.15}$$

The Gouy shift depends on the Rayleigh length, which is a measure of how quickly the beam spreads out in the transverse direction. It is therefore defined by the radius of curvature of the concave mirror.

2.2.1 Higher order modes in the microcavity

The radius of curvature in the fibre-tip R_f and the length of the cavity alone define the frequency at which the light is resonant. Knowing these two parameters, one

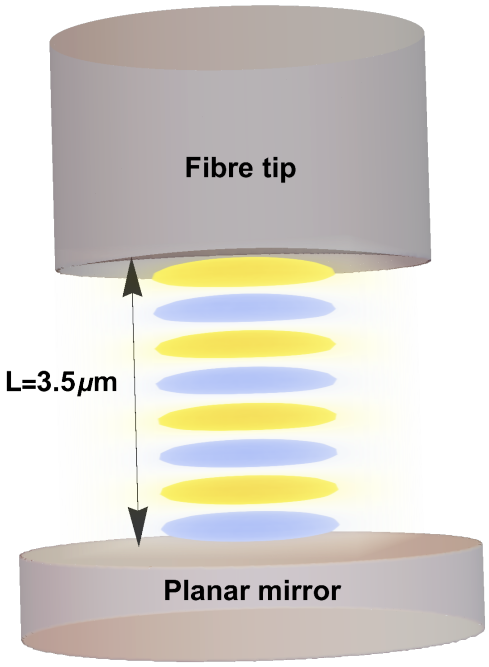

FIGURE 2.3: The zeroth-order mode in the cavity is a Gaussian beam. The beam-waist located on the surface of the flat mirror and the radius of curvature of the fibre-tip at the corresponding length L. The colour code represents the electric field component of the light oscillating in the z-direction.

can calculate the frequencies of higher orders.

$$R(L) = R_f = L\left(1 + \left(\frac{z_0}{L}\right)^2\right) \tag{2.16}$$

$$\Rightarrow z_0(L, R_f) = L\sqrt{\frac{R_f}{L} - 1} \tag{2.17}$$

$$\Rightarrow \nu_{resonance} = q\frac{c}{2L} + (n+1)\frac{c}{2L}\frac{\xi(2L)}{2\pi} \tag{2.18}$$

The structure of the resonances for a cavity with an effective length of 3.6 µm, and a radius of curvature in the fibre-tip of 35 µm, is displayed in wavelength space in figure 2.4.

2.3 Theoretical results

In order to find the optimal locking system for the microcavity, it is useful to understand which wavelength and angle of light couples into the cavity. In particular, the coupling from the Gaussian shaped beam into the zeroth, first and second-order mode are of interest. The mode matching of one Gaussian beam into another is described in [26]. The power transmission into the first and second order mode is calculated in appendix A and discussed below.

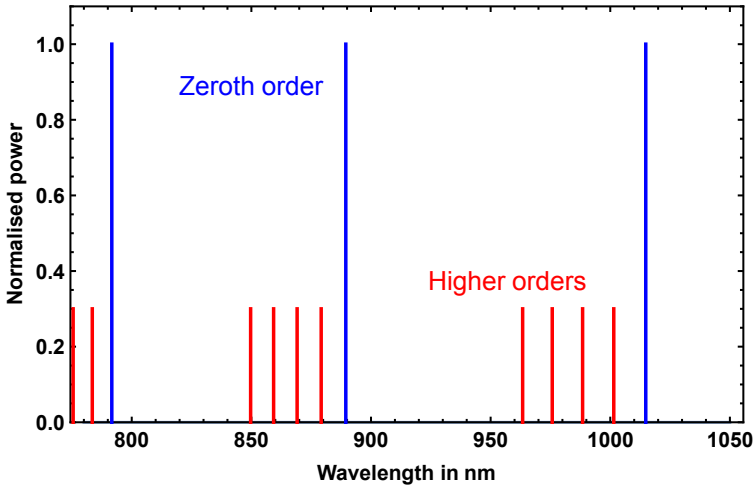

FIGURE 2.4: Here the resonant wavelength for a cavity with an effective length of 3.6 µm and a radius of curvature of 35 µm is shown. The power is arbitrarily chosen.

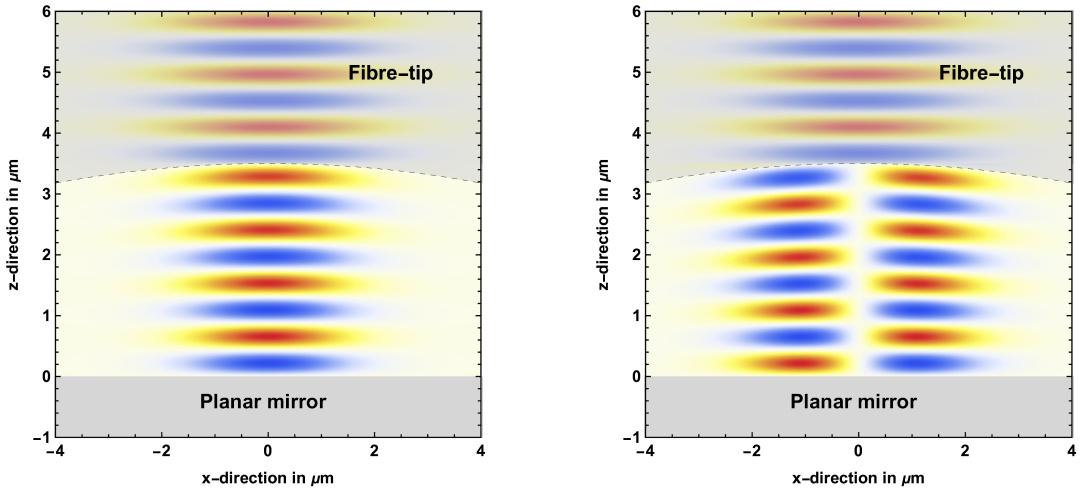

FIGURE 2.5: The incoming flat wave-front couples to the different modes in the cavity dependent mainly on the angle and the radius of curvature in the fibre-tip.

2.3.1 Mode matching into the cavity

In equation 2.18, the frequencies at which the light is resonant in the cavity are defined by q and different orders of n. Additionally, it is interesting to know how light couples from the fibre into the different orders of the resonant modes. The idea is visualised in figure 2.5. As the incoming beam can be approximated to have a flat wave-front before reaching the fibre-tip, the cavity mode must have the radius of curvature of the cavity at $z = L$, defined by the fibre-tip. In order to estimate the coupling into the cavity, the overlap integral of the incoming beam and the resonant beam profile must be solved. This can be done independently for both transverse dimensions (x, y), then generalised to three dimensions by multiplication, since the formula for the higher-order modes 2.9 is defined in that way.

0. Order	$\epsilon_{00}(\theta) = \epsilon_{00} \exp\left[-\theta^2 \epsilon_{00} \frac{k^2}{8} \left(w^2 + \bar{w}^2\right)\right]$
1. Order	$\epsilon_{10}(\theta) = \frac{k^2 \theta^2 \epsilon_{00}^2 \bar{w}^2}{4} \exp\left[-\theta^2 \epsilon_{00} \frac{k^2}{8} \left(w^2 + \bar{w}^2\right)\right]$
2. Order	$\epsilon_{20}(\theta) = \frac{1}{2}\left(\epsilon_{00} - \epsilon_{00}^2\right) \exp\left[-\theta^2 \epsilon_{00} \frac{k^2}{8} \left(w^2 + \bar{w}^2\right)\right]$

TABLE 2.1: The power transmission coefficients are dependent on the angle between the fibre and the flat mirror. The first-order mode is only populated if there is a small angle, while the zeroth and second-order always occur.

$$\left| \int_{-\infty}^{\infty} u(n, x, z, R, L, \lambda)\, u_f^*(x, z, \bar{w}, \bar{R}, \lambda) dx \right|^2 \tag{2.19}$$

The shape of the resonant beam in the cavity $u(n, x, z, R, L, \lambda)$ is known from equation 2.9. Here one can see the dependencies from the order n, on transverse position x, the position along the cavity z, the radius of curvature R, the length of the cavity L, and the wavelength of the light λ.

For light travelling through an optical fibre, the beam-waist $\bar{w}$ is roughly equal to the radius of the fibre core. The radius of curvature of the incoming beam gets reshaped by the fibre-tip. The radius of curvature of the incoming light is estimated by knowing the radius of curvature in the fibre-tip R_f, and its refractive index [27].

$$\bar{R} = \frac{R_f}{n_f - 1} \tag{2.20}$$

Using the approximations for the incoming Gaussian beam, the power transmission into the cavity modes can be calculated with equation 2.19. The exact derivations are displayed in the appendix A. The power transmission into the zeroth-order mode when the fibre is perfectly perpendicular to the flat mirror is calculated as:

$$\epsilon_{00} = \frac{4}{(\frac{\pi(n_f - 2)\bar{w}w}{\lambda R})^2 + \left(\frac{\bar{w}}{w} + \frac{w}{\bar{w}}\right)^2} \tag{2.21}$$

which matches with the results in [26]. The parameters labelled with a bar $(\bar{R}, \bar{w})$ are parameters of the incoming beam, while the unlabeled ones define the resonant mode in the cavity. The angle between the fibre and the mirror, as it is indicated in figure 2.6, is given by θ. An overview of the power transmission coefficients, in terms of the ideal zeroth-order ϵ_{00}, into the zeroth, first and second-order modes is given in table 2.1. All of the coefficients have an exponentially decaying factor $\exp\left[-\theta^2 \epsilon_{00} \frac{k^2}{8} \left(w^2 + \bar{w}^2\right)\right]$. This exponential decay indicates that the overall coupling into the cavity is reduced as the angle between the fibre and the flat mirror grows. The incoming light follows the direction of the fibre, and the part of it that couples into the cavity is the orthogonal component to the flat mirror.

The results in table 2.1 can also be used to calculate the mode matching for light coming from the flat mirror side by adjusting the values of $(\bar{R}, \bar{w})$. In figure 2.7 the power transmission in the three lowest order modes of the cavity are plotted.

By design of the cavity, the second-order mode is always excited due to the change in radius of curvature between the incoming beam and the cavity mode.

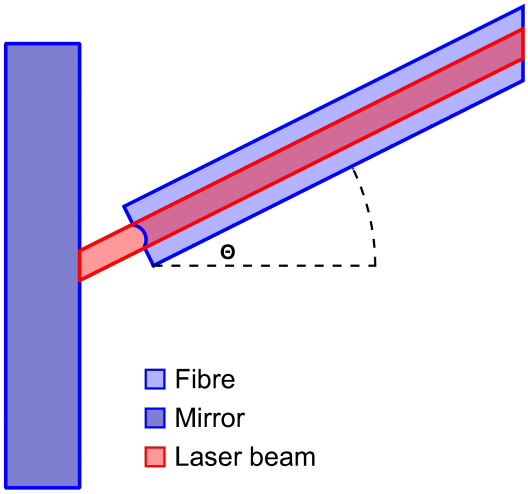

FIGURE 2.6: The angle between the fibre and the mirror strongly impacts the coupling into the different transverse order modes of the cavity.

Most of the power gets transmitted into the zeroth-order mode; this is desirable since this mode is used to perform quantum operations. The first-order is only populated if the fibre-tip has a small misalignment compared to the flat mirror; this creates an overlap between the incoming symmetric beam and the anti-symmetric first-order resonant beam.

2.3.2 The spectrum of the microcavity

Combining the results in equation 2.18 and the calculated power transmissions in table 2.1, the spectrum of a cavity can be reconstructed knowing the properties of the microcavity, as shown in figure 2.8. This plot is normalised such that the sum of the power transmissions in one free spectral range add up to one. The first three orders absorb more than 90 % of the incoming light, therefore calculating the coupling up the second-order is sufficient. One must take into account that the second-order mode is degenerate as ϵ_{02} and ϵ_{20} are both excited at the same wavelength under the assumption that the fibre-tip is symmetric. The first-order is not degenerate since it is only excited due to the misalignment angle θ. The coordinate system can be chosen so that the angle lies in the $x - z$ plane.

Studying the resonant higher-order modes reveals that it is possible to distinguish the radius of curvature and the angle of the fibre-tip to the flat mirror by comparing the power transmission through the cavity for the different resonant wavelengths forming the zeroth, first and second-orders. However, it is not trivial to compare the power of the different order modes because of their spatial distribution. By connecting a white light source to the microcavity, the spectrum can be made visible. The cavity length can be estimated using the free spectral range as the distance between two neighbouring zeroth-order resonant peaks.

$$L \approx \frac{c}{2\left(\frac{c}{\lambda_1} - \frac{c}{\lambda_2}\right)} = \frac{\lambda_1 \lambda_2}{2(\lambda_2 - \lambda_1)} \tag{2.22}$$

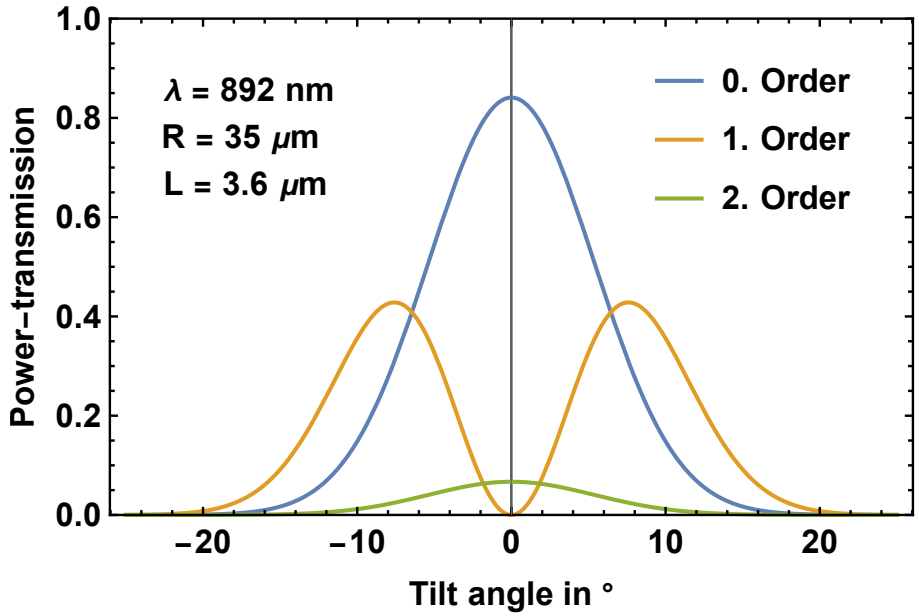

FIGURE 2.7: Due to the change in radius of curvature at the fibre-tip, the second-order transverse mode is always slightly excited. The first order is only populated if there is an angle between the fibre-tip and the mirror. As discussed in the text, odd orders are asymmetric while the incoming beam is symmetric.

In order to estimate the radius of curvature in the fibre-tip, the distances between the zeroth and first-order modes in frequency space are measured. As shown in equation 2.15, the higher orders experience a higher Gouy-shift due to their transverse expansion and, they therefore resonate at a slightly shorter wavelength. This separation depends on the length of the cavity and the radius of curvature in the fibre-tip. Using the estimated length from equation 2.22 the radius of curvature can be estimated.

$$R \approx \frac{4L}{\tan^2\left[\frac{2\pi L}{c}\delta\nu'\right]} + L \tag{2.23}$$

Here $\delta\nu' = \frac{c}{\lambda_1} - \frac{c}{\lambda_0}$ is the difference in frequency space between a first-order and neighboring zeroth-order. The radius of curvature in the fibre-tip can also be measured experimentally.

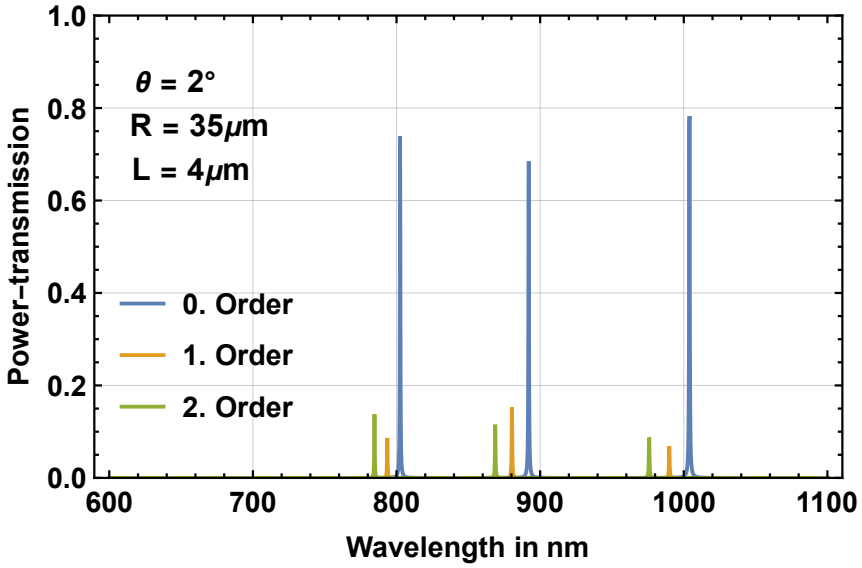

FIGURE 2.8: This plot shows the power-transmission of the light entering from the fibre at a small angle into the zeroth, first and second-order modes.

Chapter 3

Locking schemes

Reliable interaction with the rare-earth ions requires the cavity length to be stable. Therefore, passive damping in the form of a stiff and well-isolated setup is required, as well as active stabilisation to react to drifts in the system. The required length stability is estimated to be around the FWHM of the resonance peak, which is calculated knowing the finesse and the resonant wavelength [28].

$$\delta L \leq \frac{\lambda}{2\mathcal{F}} \tag{3.1}$$

For the resonant wavelength with Nd at 892 nm and a finesse of around 600 a length stability of $\delta L \approx 0.75\,\text{nm}$ is required. In order to increase the Purcell enhancement, the next generation microcavity setup will have a finesse of around 6000; therefore, the stability needs to be in the tens of picometer range.

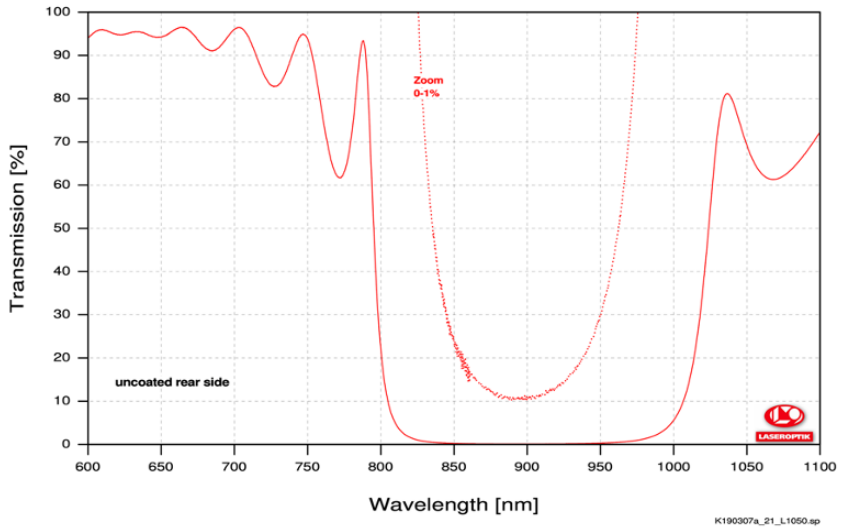

FIGURE 3.1: The transmission of the fibre-tip coating is minimal between 850 nm and 950 nm so that the main wavelength of 892.16 nm is centered in this range. The graph was provided with the fibres from *LASEROPTIK GmbH*.

In this work, different techniques for actively stabilising microcavities are discussed. To re-correct the fibre position after a change in length, the fibre is mounted onto a shear-piezo. The piezo crystal is controlled by a feedback loop connected to the detection scheme, which observes the length of the cavity. When discussing the

possible schemes, it must be considered that the main purpose of the cavity is to enhance the read-out of rare-earth ions. An ideal locking scheme would not interfere with the experiment.
Another limitation of the locking is dictated by the reflectivity coating of the mirror and the fibre-tip. The information about the coatings is displayed in figure 3.1 which shows that the high reflectivity ranges from 850 nm to 950 nm. Comparing these values to the spectrum shown in figure 2.8, it is clear that when the main resonance is tuned to the excitation wavelength of Nd at 892.16 nm the higher and lower resonance zeroth-order peaks are outside of the high reflectivity range [29]. Therefore, the locking scheme needs to rely on the same wavelength as the optical transition of Nd or take advantage of the higher-order modes.

3.0.1 Side-of-fringe locking

Side-of-fringe locking uses power transmission as an error signal. The power transmitted through the cavity is maximised when the laser light is in resonance with the cavity length; by slightly detuning the cavity length with respect to the wavelength, the measured power of the transmitted light decreases. Starting at the resonance peak, a decrease in power does not indicate in which direction the cavity length has shifted. In order to get this information, the locking scheme must not lock the cavity to the top of the fringe. Rather, it uses the steepest slope on one side of the fringe as the error signal. The power increases if the length shifts towards the peak and decreases in the other direction. This is indicated in figure 3.2.

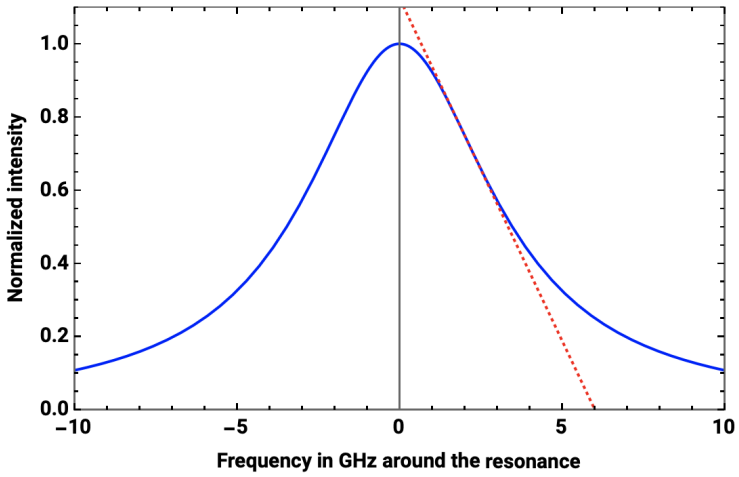

FIGURE 3.2: The transmission signal of the cavity with respect to frequency detuning. The red line indicates the maximal derivative.

Side-of-fringe locking has some advantages due to its simplicity. The laser light used for the locking does not have to be modulated, and the detection of the error signal requires only a photo-detector. The precision in time is limited by the detector and the response-time of the cavity, which is naturally extremely short for microcavities.

The optimal error signal is obtained when the cavity is locked to the steepest point of the Lorentzian function describing the transmission signal. The transmitted

intensity as a function of frequency ν for one resonance peak is:

$$I(\nu) = \frac{\Gamma^2}{\Gamma^2 + (\nu - \nu_0)^2} \tag{3.2}$$

where ν_0 is the resonant frequency and Γ is the FWHM. To get the best response in the error signal, the laser should be locked to the frequency where the derivative of the intensity is maximized.

$$\nu_{lock} = \nu_0 \pm \frac{\sqrt{3}}{3}\Gamma \approx \nu_0 \pm \frac{\sqrt{3}}{6}\delta\nu \tag{3.3}$$

The responsiveness of the error signal is estimated as the maximal derivative of the Lorentzian.

$$\frac{dI}{d\nu}(\nu_{lock}) = \frac{3\sqrt{3}}{8\Gamma} \approx \frac{3\sqrt{3}}{4}\frac{1}{\delta\nu} \tag{3.4}$$

The main disadvantages of side-of-fringe locking are that power fluctuation in the light source directly translates into the error signal and that it can not lock the cavity to the top of the fringe. In a noisy environment, the locking position would jump from one side of the slope to the other, making it impossible to lock.

3.0.2 Pound–Drever–Hall locking

The PDH locking technique is widely used for laser locking and is very famously applied to detect the gravitational waves where infinitesimal changes in the cavity length are detected, as was already proposed by Drever in 1983 [30]. The technique is based on the phase shift, which is induced in the light inside the cavity if the length of the cavity is slightly detuned with respect to the wavelength and phase of the incoming light [8]. This phase shift is indicated in figure 3.3. This plot shows the power and the phase of the reflected light depending on the frequency in terms of the free spectral range.

The PDH scheme is based frequency-modulated light, which interferes with the light entering the cavity to generate the error signal. Through modulation of the laser beam, two sidebands are excited, which are not affected by the cavity since they are outside of the resonance peak, acting as a reference signal.

The signal of the central beam enters the cavity while the two sidebands get mostly reflected in the optimal PDH-locking. The light that has entered the cavity experiences a phase shift due to detuning in the cavity length regarding the frequency of the resonating light. The light inside the cavity leaks out of the cavity on both sides. The cavity perfectly aligns with the incoming laser light if the directly reflected light exactly cancels with the light leaking out of the cavity. The reflected light is described by the complex reflectivity as displayed in figure 3.3.

$$f_r(\omega) = \frac{E_{ref}}{E_{inc}} = \frac{r\left(e^{\frac{i}{c}2L\omega} - 1\right)}{1 - r^2 e^{\frac{i}{c}2L\omega}} \tag{3.5}$$

In [8] the PDH error signal using reflection is derived in detail.

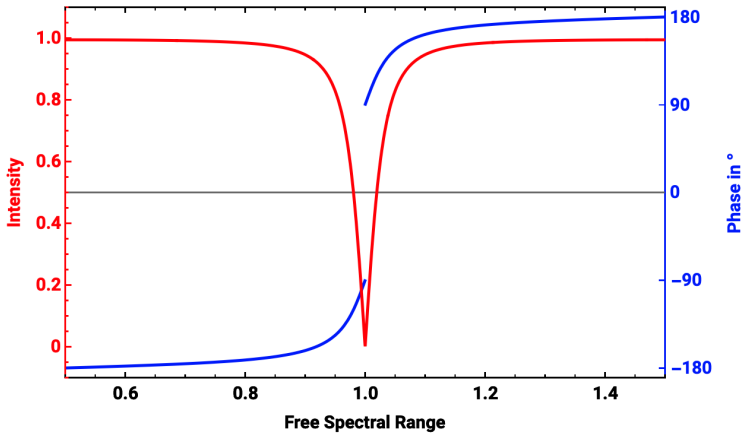

FIGURE 3.3: The complex reflection from a cavity is dependent on the incoming light. A small mismatch between the cavity length and the wavelength of the incoming light induces a phase shift into the reflected and transmitted light, as shown by the blue curve. This phase shift induces the error signal of the PDH locking.

PDH in transmission

In the case of microcavities, the resonance peaks are so broad that the sidebands are inside the resonance peak so that they enter the cavity. Nevertheless, they are slightly less affected by cavity length changes than the main beam, such that an error signal is created. Since the sidebands pass through the cavity, the error signal in the transmission signal has a comparable magnitude as the reflected error signal, as shown in figure 3.4.For example, suppose that the error signal is detected in the transmitted light on the other side of the plane mirror. In that case, the microcavity acts as a filter so that unwanted etalon effects in the fibre coupling are suppressed.

The transmitted electric field of an optical cavity can be written as:

$$\frac{E_{trans}}{E_{inc}} = -\frac{t_1 t_2}{\sqrt{r_1 r_2}} \frac{\sqrt{g(\omega)}}{1 - g(\omega)} \tag{3.6}$$

following the derivations in [24]. In this equation, t and r are the field transmission and reflectivity. The amplitude transmission is defined as $t^2 = 1 - r^2$ where $r_1 = r_2 = r$. $g(\omega)$ is known as the round–trip–voltage–gain.

$$g(\omega) = r^2 \exp\left(-\alpha * 2L - i\omega 2L/c\right) \tag{3.7}$$

α represents the internal losses in the cavity which are not considered in the further calculations. The incoming modulated beam is described as:

$$E_{inc} = E_0(J_0(\beta)e^{i\omega t} + J_1(\beta)e^{i(\omega+\Omega)t} - J_1(\beta)e^{i(\omega-\Omega)t}) \tag{3.8}$$

here E_0 is the electric field amplitude, J represents the Bessel functions of the first kind and β is describing the modulation depth. This modulation depth determines how much of the laser beam gets transferred from the centre-frequency ω to the sideband frequencies $\omega \pm \Omega$ [8].

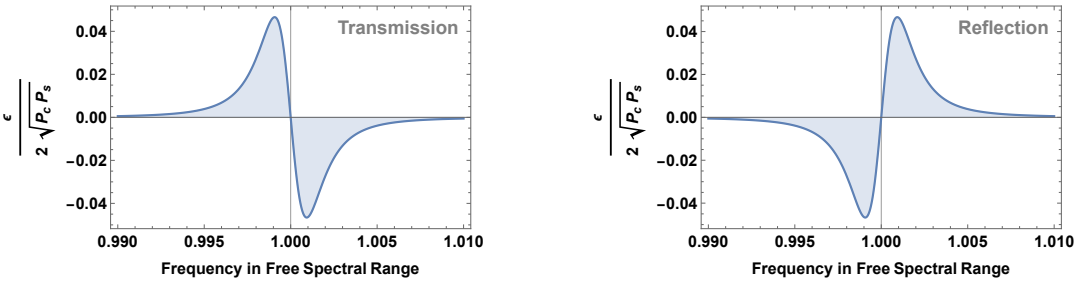

FIGURE 3.4: The error signal of the PDH locking for short cavities with a wide resonant peak is almost equivalent in reflection and transmission. The transmitted error signal has the advantage that the cavity filters the light in all other wavelengths. These plots display the dominant real part of the error signal for a cavity length corresponding to four times the wavelength (approximately 3.5 µm) and finesse of around 630.

For simplification it is convenient to define the complex transmission $f_t(\omega)$ in analogy to the complex reflection $f_r(\omega)$.

$$f_t(\omega) = \frac{E_{tras}}{E_{inc}} = \frac{(1-r^2)e^{\frac{i}{c}L\omega}}{1-r^2e^{-\frac{i}{c}2L\omega}} \tag{3.9}$$

Therefore, the transmitted field can be rewritten as follows.

$$E_{trans} = E_0\left[-f_t(\omega)J_0(\beta)e^{i\omega t} - f_t(\omega+\Omega)J_1(\beta)e^{i(\omega+\Omega)t} + f_t(\omega-\Omega)J_1(\beta)e^{i(\omega-\Omega)t}\right] \tag{3.10}$$

The transmitted power is calculated as $P_{trans} = |E_{trans}|^2$.

$$\begin{aligned} P_{trans} &= P_c|f(\omega)|^2 + P_s\{|f(\omega+\Omega)|^2 + |f(\omega-\Omega)|^2\} && (3.11)\\ &+ 2\sqrt{P_cP_s}\{\mathbf{Re}[f(\omega)f^*(\omega+\Omega) - f^*(\omega)f(\omega-\Omega)]\cos\Omega t && (3.12)\\ &+ \mathbf{Im}[f(\omega)f^*(\omega+\Omega) - f^*(\omega)f(\omega-\Omega)]\sin\Omega t\} && (3.13)\\ &+ (2\Omega \text{ terms}) && (3.14)\end{aligned}$$

The error signal oscillates with the frequency Ω and has and the amplitude of $f(\omega)f^*(\omega+\Omega) - f^*(\omega)f(\omega-\Omega)$. When two times the modulation frequency is smaller than the spectral width; the sidebands are inside the resonance peak, and the error signals from transmission and reflection are similar.

Slope of the PDH error signal

In order to compare the different locking schemes, it is convenient to estimate the slope of the error signal around the locked position. To calculate the slope of the error signal, the approximation for slow modulation with respect the spectral width given in equation 3.15 is a valid starting point [8].

$$\epsilon = 2\sqrt{P_cP_s}\frac{d|f_r|^2}{d\omega}\Omega \tag{3.15}$$

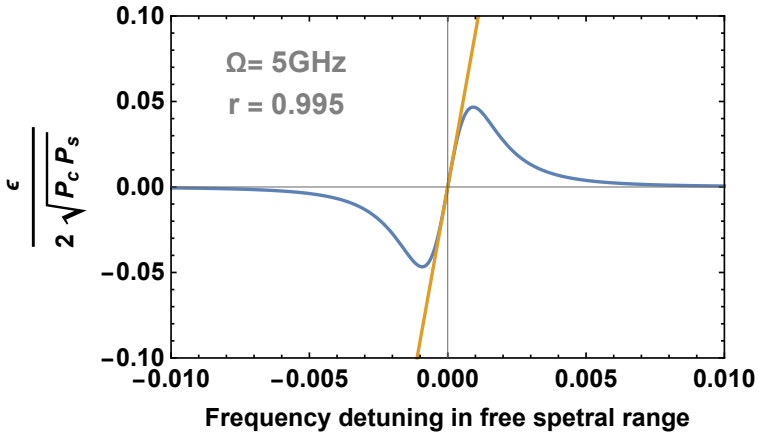

FIGURE 3.5: The slope of the PDH error signal around the resonance frequency can be approximated by a linear function which gives the signal per frequency displacement. Here the error signal is plotted for a cavity length corresponding to four wavelengths (around 3.5 µm) with a finesse of around 630 where the sidebands are modulated with 5GHz.

$$|f_r|^2 = \frac{2r^2(1-\cos(\frac{\omega}{\Delta\nu}))}{1+r^4-2r^2\cos(\frac{\omega}{\Delta\nu})} \tag{3.16}$$

To approximate the linear behaviour of the error signal, around the perfectly aligned cavity, the function ϵ was Taylor expanded to the first-order around $w = 2\pi\Delta\nu$.

$$\epsilon \approx 2\sqrt{P_c P_s}\frac{4\pi r^2}{(r^2-1)^2\Delta\nu^2}\Omega\omega \tag{3.17}$$

For better comparison with the side-of-fringe slope, it is convenient to write the slope in terms of the spectral width $\delta\nu$ as it is done in the case of side-of-fringe locking.

$$\frac{dI}{d\nu} \sim \frac{\Omega}{\delta\nu}\frac{1}{\delta\nu} \tag{3.18}$$

The approximation fits the error signal around the zero-crossing as shown in figure 3.5.

3.0.3 Tilt locking

Tilt locking is based on the overlap of symmetric and asymmetric solutions of the paraxial wave equation [9]. One complete set of solutions are the Hermite–Gaussian higher-order modes given in equation 2.9. The even-orders of the Hermite functions are spatially symmetric functions, while the odd orders are asymmetric functions along the transverse axis. Tilt locking takes advantage of the first and zeroth-order spatial mode to monitor the length changes of cavities.

The electric field components along the transverse axis are displayed in figure 3.6. The corresponding power is symmetric for both orders independently because the power is the electric field squared, as shown in figure 3.7.

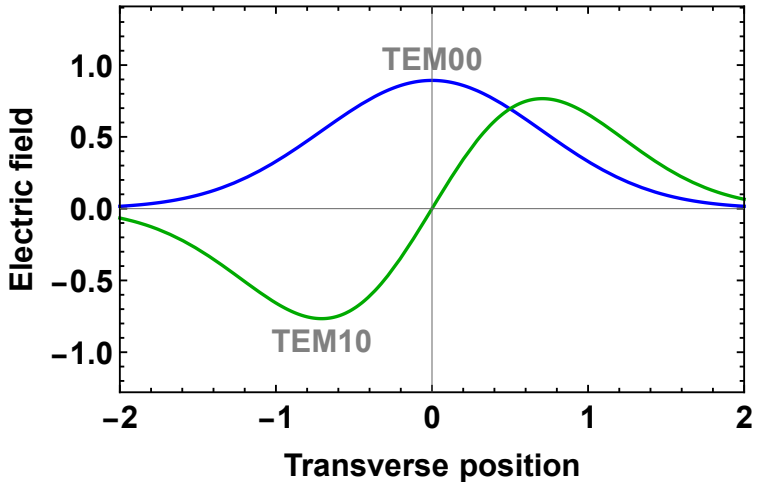

FIGURE 3.6: The electric field of the zeroth-order (TEM00) here in blue is a symmetric function along the transverse plane, while the first order (TEM10) component has an asymmetric shape along the transverse axis.

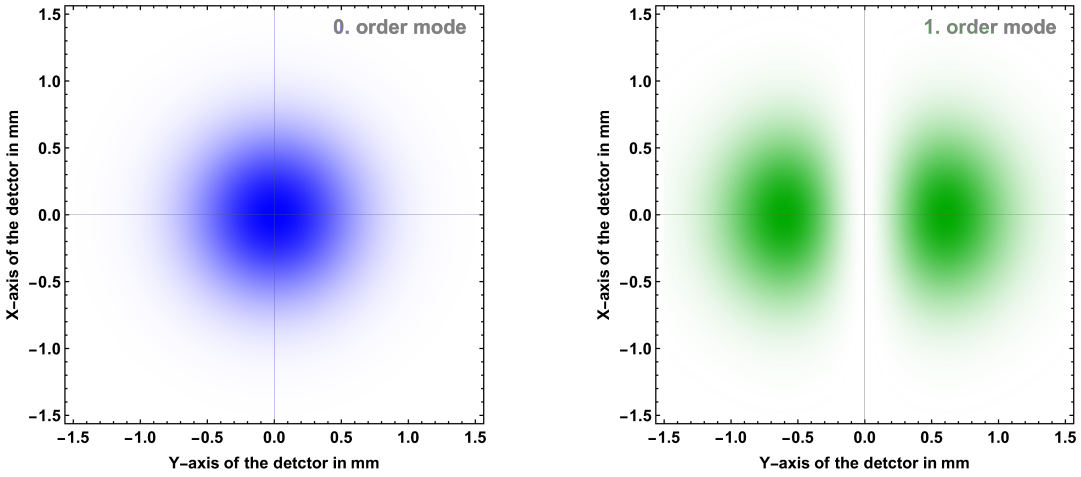

FIGURE 3.7: These plots show the power distributions of the zeroth (blue) and first (green) order respectively. The simulation is done for a detector capturing the transmission signal of the cavity 5mm behind the flat mirror with a cavity length of 4 times the wavelength (around 3.5 µm).

Higher-order modes are resonant for slightly different lengths of the cavity due to the additional Gouy-shift as discussed in detail in chapter 2.2.1. Therefore, when the cavity is resonant to the first-order mode, the asymmetric part of the incoming beam enters the cavity. The zeroth-order is not resonant to that cavity length. The symmetric part of the beam does not entering the cavity but directly reflected. That means that the asymmetric part of the incoming beam is amplified by the cavity and is affected by the phase shift, while the symmetric order stays unaffected. In this case, the symmetric part of the light acts as the reference signal in analogy with the sidebands in the PDH technique. For the microcavity in our setup, the separations between the transverse modes are in the order of nm as discussed in 2.2.1.

Tilt locking makes use of the phase shift induced in resonant light as the cavity drifts out of resonance.

$$f_r(\omega) = \frac{r\left(\exp\left(i\frac{\omega}{\Delta\nu}\right) - 1\right)}{1 - r^2\exp\left(i\frac{\omega}{\Delta\nu}\right)} \tag{3.19}$$

This complex reflection is shown in figure 3.3. The reflected beam consists of the first-order mode, which is amplified in the cavity and experiences the phase shift when slightly out of resonance. Meanwhile the zeroth transverse order is off-resonance at the chosen wavelength and gets reflected by the flat mirror. The electric field of the reflected light can be approximated by:

$$E_{ref} = f_r(\omega_{00})u_{00} + \frac{i\pi\theta\omega_0}{\lambda} f_r(\omega_{10})u_{10} \tag{3.20}$$

$$= f_r(\omega_{00})u_{00} + \frac{i\pi\theta\omega_0}{\lambda} f_r(\omega_{10})\frac{2x}{\omega(z)}\exp\left[i\xi\right]u_{00} \tag{3.21}$$

with the assumption that θ is a small tilt angle [31]. The power of the beam is calculated as the absolute electric field squared.

$$P_{ref} = |f_r(\omega_0)|^2|u_{00}|^2 + |f_r(\omega_1)|^2|u_{00}|^2\frac{2x^2\pi^2\theta^2\omega_0^2}{\lambda^2\omega(z)^2} + \tag{3.22}$$

$$\frac{2x\pi\omega_0\theta}{\lambda\omega(z)}|u_{00}|^2 i\left\{f_r^*(\omega_{00})f_r(\omega_{10})\exp\left[i\xi(z)\right] - f_r^*(\omega_{10})f_r(\omega_{00})\exp\left[-i\xi(z)\right]\right\} \tag{3.23}$$

The last term is responsible for the error signal. It is the phase-shifted first-order contribution interfering with the none phase-shifted symmetric beam. To identify this signal a split-detector can be used. To measure the power of the out-coming beam independently for $0 \to \infty$ and $-\infty \to 0$ the detector should be placed in the centre of the light leaking out of the cavity. The two maxima of the intensity distribution of the first-order mode, as shown in figure 3.7, should match the orientation of the split detector. The error signal is the subtraction of the two measured powers.

$$Error = \int_{\infty}^{\infty}\int_{0}^{\infty} P_{ref}(x)\,dx\,dy - \int_{\infty}^{\infty}\int_{-\infty}^{0} P_{ref}(x)\,dx\,dy \tag{3.24}$$

A simulation of the tilt locking error signal is displayed in figure 3.8. The length of the cavity is scanned over the zeroth and first-order resonance. At both resonances, the error signal spikes with the characteristic steep slope, which can be used to lock the cavity. In the simulation, it shows that the shape of the length-dependent curves representing the power of the two sides of the detector differs for the first and zeroth-order resonance.
In figure 3.9 only the behaviour directly around the resonances is displayed. For the first-order resonance, the light reshaped by the cavity has two peaks with a phase-difference of 180°; therefore, one of them will constructively interfere with the symmetric reflected light while the other one destructively interferes. In the case of the resonant zeroth-order, the incoming beam is slightly tilted while the wave-front of the resonant light is perfectly parallel to the flat mirror. Therefore, there is a certain angle, dependent on the tilt of the beam between the light resonant with the cavity and the directly reflected light. Thus, a phase change in the cavity can be seen along the transverse axis as shown in figure 3.8 in the form of a phase shift between the

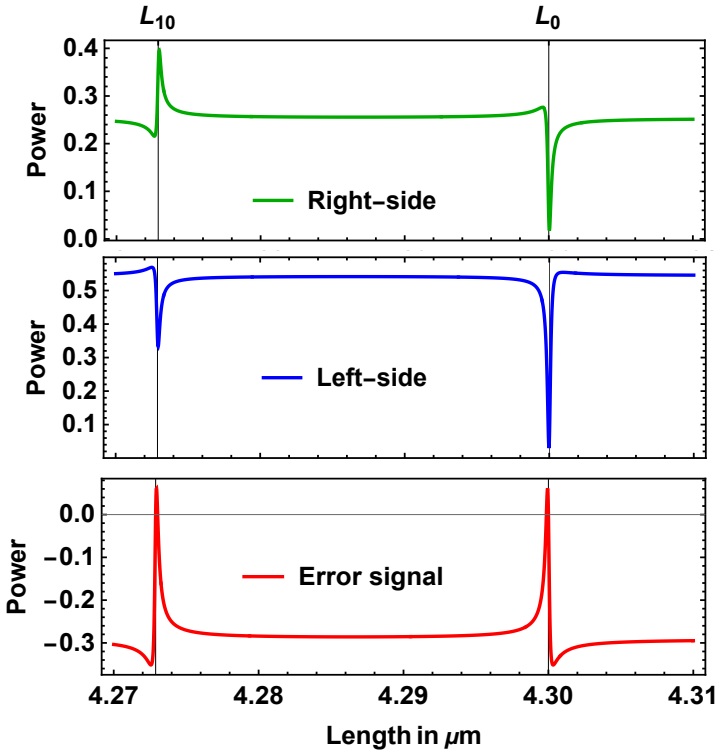

FIGURE 3.8: Here, a simulation of the error signal which could be acquired with the tilt locking technique is displayed. The laser light has a wavelength of 860 nm, the cavity has a finesse of around 3000. The detection plane was chosen to be one Rayleigh length (around 10 µm) behind the beam waist at the flat mirror. The first spike in the error signal (red curve) occurs at the cavity length, which is resonant to the first-order around 4.27 µm while the zeroth-order is resonant at 4.3 µm. When looking at the curves representing the two detector sides, one can see that the behaviour differs for the first-order and zeroth-order resonances.

two dips corresponding to the two sides of the detector.

3.1 Comparing different locking schemes

When discussing suitable locking schemes for microcavities, the limitations need to be taken into account. Firstly, due to the short length of the cavity, the free spectral range and the spectral width are broad because of their one over L dependence. Secondly, the coating limits the high reflectively range. In this case, the reflectivity range only covers one spectral range.

As side-of-fringe locking is already installed into the current setup, it makes sense to compare possible options with it. As discussed above, side-of-fringe locking locks the cavity length slightly off from the peak of the cavity transmission; thus, when using this technique, one cannot use the full potential of the cavity enhancement. Additionally, the locking laser has the same wavelength as the laser used for the ion interactions. This means that one can use the same light source for both

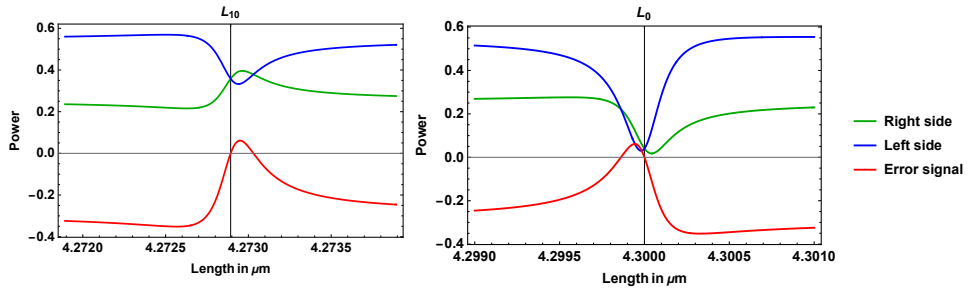

FIGURE 3.9: This simulation focuses on the behaviour around the zeroth (on the right) and first-order (on the left) resonance. When passing the resonant length of the first-order, the power on the two sides of the detector spike in the opposite direction.

applications, but on the other hand, one has to turn off the locking when doing experiments on the ions. This timing is not a problem as the interaction time with the ions is shorter than the piezo crystal response time, which corrects the cavity length. The disadvantage is that one needs to wait for the locking scheme to ensure the correct length of the cavity after each ion interaction.

Using the PDH scheme would overcome the main disadvantage of side-of-fringe locking as it locks the cavity to the top of the fringe. This method is based on interfering resonant light with an off resonant reference signal. In order to create this reference, the light is modulated to have two sidebands. In contrast to the side-of-fringe locking, the laser power fluctuation does not translate directly into the error signal. On the downside, due to the short distance between the mirrors of the cavity, the spectral width is large following $\delta\nu \sim \frac{1}{L}$. When directly comparing the slope of the error signal expected for PDH (equation 3.18) and side-of-fringe, (equation 3.4) one can see that the slope of the PDH scheme only has a better response when $\Omega > \delta\nu$. In our case, the spectral width is in the order of $\delta\nu \sim 60 \times 10^9$, which would mean that a 60 GHz modulation frequency would be required. This high modulation is not practical since modern electro-optical modulators and detectors in this frequency range are very expansive and the noise of a detector scales up with the detection frequency; thus, PDH locking is only feasible if one increases the finesse by an order of magnitude to decrease the spectral width.

Two potential ways to lock the cavity continuously without disturbing the ion interaction are discussed. The light used for locking can either be separated spatially or in frequency to distinguish between the locking and the ion interactions. To separate the locking spatially, it has been demonstrated that one can lock the length of a fibre-based cavity by glueing another fibre to it, exclusively used for the locking scheme [32]. This method of using two fibres has the advantage that the fibre that forms the cavity for the ion interactions can operate continuously. One could lock the second one so that the main fibre cavity is on top of the fringe. The disadvantage of this method is that long term thermal drifts between the two fibres still require the re-locking of the main fibre after some time as discussed in [32]. Additionally, assembling the two fibres in the experimental setup and controlling them independently is experimentally challenging.

Instead of separating the light used for locking and for the ion interaction spatially, one could use separation in frequency. While the free spectral range exceeds the reflective range of the mirrors, the higher-order modes of the cavity are always

inside this range. The first-order mode resonates at around a 10 nm shorter wavelength as derived in chapter 2. This difference is sufficient to separate the light in the detection to be able to run consciously without disturbing the ion read-out. When combining either side-of-fringe or PDH locking with using the higher-order mode, the error signal would be multiplied by the coupling coefficient into that higher-order mode. This coupling coefficient is for a reasonable angle below 0.2 and, if one would use the second-order, below 0.1 as displayed in 2.7.

As derived above, tilt locking creates a similar error signal around the first-order mode as it does for the main resonance; thus, tilt locking can lock the first-order mode without a drawback, while the main resonance is used to interact with the ions. The slope of the error signal created by tilt locking is the subtraction of two transmission peaks spiking in opposite directions. In contrast, the total transmission, which is the base for side-of-fringe locking, corresponds to the addition. The simulated results displayed in figure 3.10 show that the error signal around the zeroth-order resonance is comparable to the slope of the side of the fringe. When the length of the cavity is passes the first-order resonance, the fringe is decreased, which corresponds to the error signal of side-of-fringe locking.

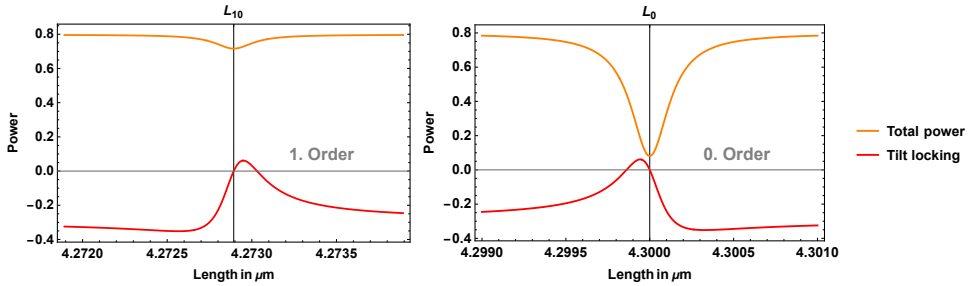

FIGURE 3.10: In this plot, the power measured by the two sides of the split detector are added here in orange and subtracted in red. In the right plot, the behaviour around the zeroth-order mode is shown. In the left plot, the cavity length passes the first-order resonance.

Tilt locking is based on the same principle as PDH locking, namely using the cavity length-dependent phase shift interfering with a reference signal to monitor the length changes. The difference is that the reference signal of tilt locking is well outside the spectral width. It does not require a modulator. The main drawback of the tilt locking scheme is that it needs to be done from the mirror side of the cavity because the fibre creating the cavity is a single-mode fibre and would suppress the first-order mode.

Chapter 4

Experimental methods

4.1 Overview optical setup

To test the tilt locking technique's functionality to stabilise a microcavity, a test setup was built. The goal was to mimic the setup that is currently being built for the cryostat. The same coated fibres and the highly reflective mirror are used to create the microcavity in the test setup to make it comparable.

In order to meet the stability condition of the microcavity, the fibre-tip must be closer to the mirror than the radius of curvature in the fibre-tip. The coating of the fibre-tip is susceptible to damage. It breaks if there is an abrupt physical interaction with the mirror; thus, the fibre-tip is mounted on a micrometre stage. This stage allows for moving the fibre-tip close enough to the mirror to form the microcavity in a controlled way. The needle onto which the fibre-tip is glued is mounted on a PL5FBP3 shear piezo chip from *THORLABS*. A conceptual overview of this is shown in figure 4.1.

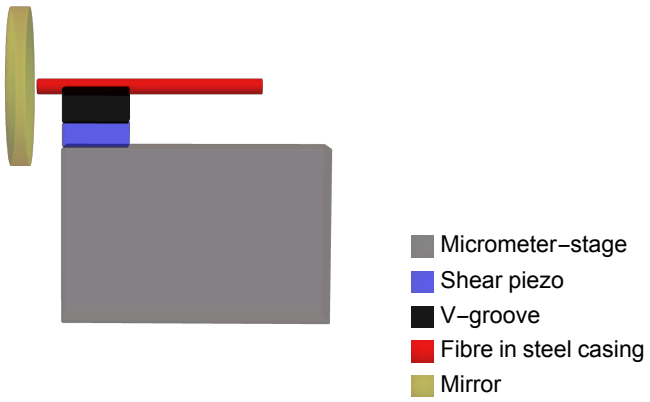

FIGURE 4.1: The figure is out of proportion but gives a clear idea of how the fibre-tip is mounted. The shear piezo has a theoretical range of up to 1.3 µm while the micrometre-stage has a range of a few mm. The fibre needs to be less than 10 µm away from the flat mirror.

As discussed in appendix B, the expansion of the beam waist leaving the cavity is defined by the spatial dimension of the cavity and rapidly expands after it passes the mirror. The beam needs to be refocused directly behind the mirror to get the signal out of the setup without cutting off the higher-order spatial modes. In this setup, the aspheric lens *A240-B* from *THORLABS* is used, which has an effective working distance of 5.92 mm and a clear aperture with a diameter of 8 mm. The high reflectivity mirror from *LASEROPTIC* is 3 mm thick. The focus point of the

cavity is directly on the surface of the flat mirror. Therefore, the lens must be placed about 2.9 mm behind the mirror. The lens is mounted on another micrometre-stage to control its exact position in all three dimensions.

The general setup of the experiment is shown technically in 4.2. After passing through an optical adjustment setup of two mirrors to have control of the height and transverse position of the beam, the laser light is focused on the cavity by the aspheric lens. A beam splitter redirects the reflected beam and the light coming from the cavity towards the detector. The 10/90 beam splitter is set up so that 90 % of the light from the cavity reaches the detector.

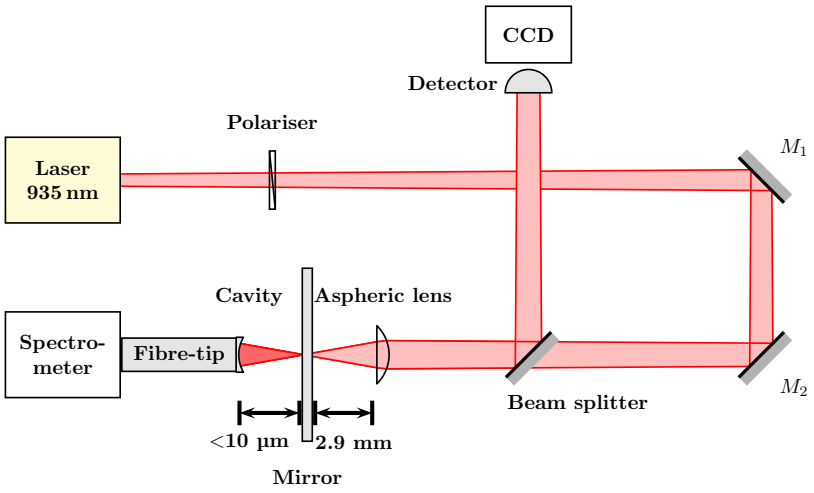

FIGURE 4.2: The setup was designed to be similar to the actual setup inside the cryostat. The cavity consists of the same fibre and coated mirror. The laser light has a wavelength of 935 nm which is in the high reflection range of the mirror and fibre coating. When looking at the beam profile, the detector is interchanged with a CCD camera.

To control the polarisation of the light coming from the laser, a B-coated "Glan-Laser Calcite Polariser" from *THORLABS* with an extinction ratio of $10^6 : 1$ is mounted in a rotation stage just in front of the laser. Setting the polarisation is helpful in maximising the signal-to-noise ratio, as only a certain polarisation couples into the cavity which is an effect known as the Brewster's angle. This is especially the case for the asymmetric spatial modes.

The split-detector is mounted on a micrometre stage which is adjustable along the transverse axis of the incoming beam. The detector itself is placed into a rotatable holder to adjust the splitting axis of the detector. A QP5.6-TO5 quad pin detector from *first sensor* was chosen because of its low dark current and the narrow gap between the elements of just 24 µm. It has four elements with an active area of 1.22 mm^2 each.

The simple electrical setup, used to read out the two sides of the split detector and subtract them, is shown in figure 4.3. The detector is powered with a reverse voltage between 20 V and 30 V. The two sides of the detector are connected to a 150 kΩ resistor across which an oscilloscope measures the voltage. The oscilloscope is operated in AC mode to remove the constant offset due to directly reflected light. In order to display the error signal, the two channels of the oscilloscope are subtracted using the math menu.

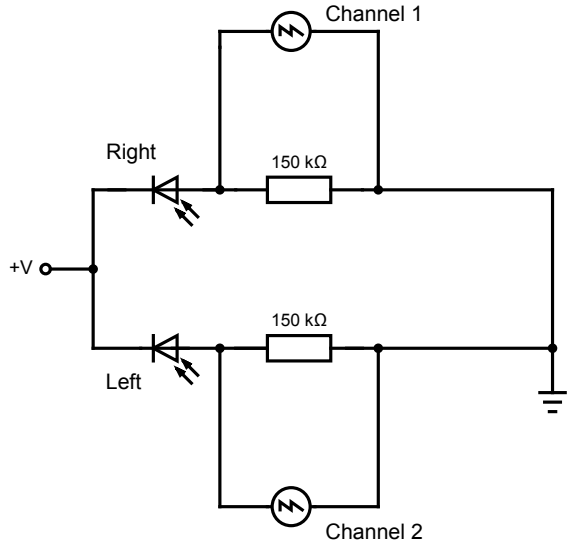

FIGURE 4.3: To have a simple readout option for the split detector, the two sides of the detector are connected to resistors. Two channels of an oscilloscope read out the voltage over the two resistors. The detector is operated with a reverse voltage of 20 V to 30 V.

The light from the resonant cavity and the directly reflected light need to overlap to measure an error signal. It is helpful to place a CCD camera in front of the detector to check this overlap. The camera allows for monitoring the beam profile of the cavity modes and thereby set the axis of the split detector to match the axis of the first-order mode. In this setup, the DCC1545M monochrome sensor from *THORLABS* is used. This sensor has an active area of 6.66 mm $\times$ 5.32 mm.

As a light source a DFB laser from *nanoplus* with a center-wavelength of 935 nm was installed. This laser has a power output of up to 20 mW and a FWHM of around one nanometer. 935 nm is a suitable wavelength concerning the high reflectivity range of the mirror, and the linewidth is smaller than the separation between the zeroth and first-order cavity mode. This laser is not sufficient for the actual locking system when the ions are targeted because of the missing tunability and the wrong wavelength with respect to the Nd ion transition, but it was available in the lab and sufficient to build this proof of principle test setup.

A spectrometer is connected to the end of the fibre forming the cavity. The spectrometer monitors the coupling into the cavity. In this setup, the AvaSec-ULS4096CL-EVO from *AVANTES* is installed. In order to measure an error signal, the cavity needs to be sufficiently stable so that the cavity length does not drift off immediately. The whole setup is mounted onto a floating optical table to meet the stability requirements.

4.2 Aligning and initialising

The fibre-tip is extremely sensitive, and one needs to be careful not to destroy the high reflectivity coating; thus, it is crucial to monitor the distance between the fibre-tip and the flat mirror when adjusting the micrometre-stage to form the cavity. For this purpose, a white light source that has a wavelength span from 600 nm to 1100 nm is connected to the cavity fibre. The spectrometer is positioned on the flat-side of the

cavity to observe the fringe pattern of the microcavity. Once the distance between the fibre-tip and the mirror is short enough to meet the stability condition, the fringes of the cavity appear on the spectrometer, as shown in figure 4.4.

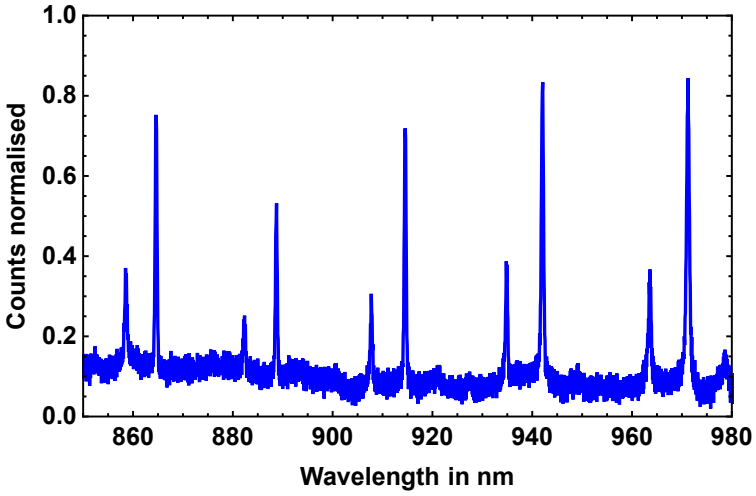

FIGURE 4.4: When shining with a white light source onto the cavity, one can observe its spectrum. The distance between two zeroth-order resonances is measured to estimate the length of the cavity. In this spectrum, one can see the zeroth and first-order modes of the cavity with a length of about 13 µm.

The length of the cavity is estimated by measuring the distance between two zeroth-order resonances as derived in chapter 2.3.2. Knowing the distance between the fibre-tip and the mirror, it is possible to slowly decrease it with the micrometre-stage until reaching the length regime of interest below 10 µm. The fibre is moved until a zeroth or first-order resonance peak reaches 935 nm.

As soon as an overlap of the first-order resonance and the laser is detected, the white light source is removed, and the spectrometer gets directly connected to the cavity fibre. Now the laser is focused on the cavity coming from the mirror-side. The transmission is monitored with the spectrometer. A good coupling into the first-order resonance mode is shown in 4.5. This plot clearly shows that it is possible to sufficiently focus the laser beam through the mirror into the cavity and excite the first-order cavity mode.

Only light with particular polarisation couples into the first-order mode; thus, the polariser can filter out light that cannot couple into the cavity. In this way, the signal-to-noise ratio of the error signal is improved because it decreases the amount of reflected light.

To be able to detect the tilt locking error signal, the light of the first-order and the reflected symmetric beam need to overlap at the split detector. By placing the CCD camera in front of the split detector, the first-order is observable when the laser is directly connected to the cavity fibre. When the laser approaches the cavity from the mirror-side, the CCD camera detects the reflected Gaussian-shaped beam, which should spatially overlap with the cavity mode. The results of this scheme are discussed in chapter 5. This result is also important in order to see the orientation of the first-order and to rotate the split detector accordingly.

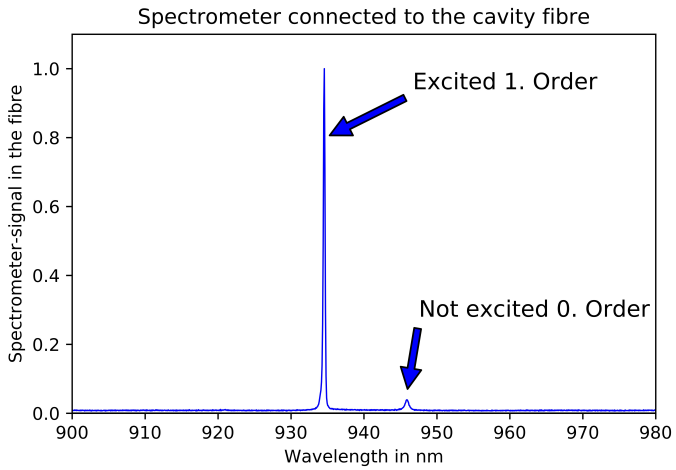

FIGURE 4.5: The first-order mode is excited by the 935nm laser which enters the cavity from the mirror-side. The zeroth order is slightly excited because the tail of the laser in this setup is very large and covers this wavelength. This shot is taken by the spectrometer which is connected to the fibre.

4.3 Creating the error signal

In order to create an error signal, the shear piezo under the fibre-tip is connected to a function generator to drive the fibre-tip back and forth. The signal is amplified with a gain of 25 V/V to create a sufficient offset in the length of the cavity. The TD250 from *PiezoDrive* is used here. The two sides of the detector are connected to the oscilloscope HDO6104A from *LeCroy* while the trigger is directly connected to the function generator.

The oscilloscope is operated in AC mode to be able to zoom in on the error signal despite the offset-voltage resulting from the directly reflected light. To calculate the error signal, the math option of the oscilloscope subtracts channel one from channel two. With the aim to find the optimal error signal, the split detector is slowly moved along the transverse axis until the signal from the right and left side of the detector is approximately equal. A photo of the optical setup is presented in figure 4.6.

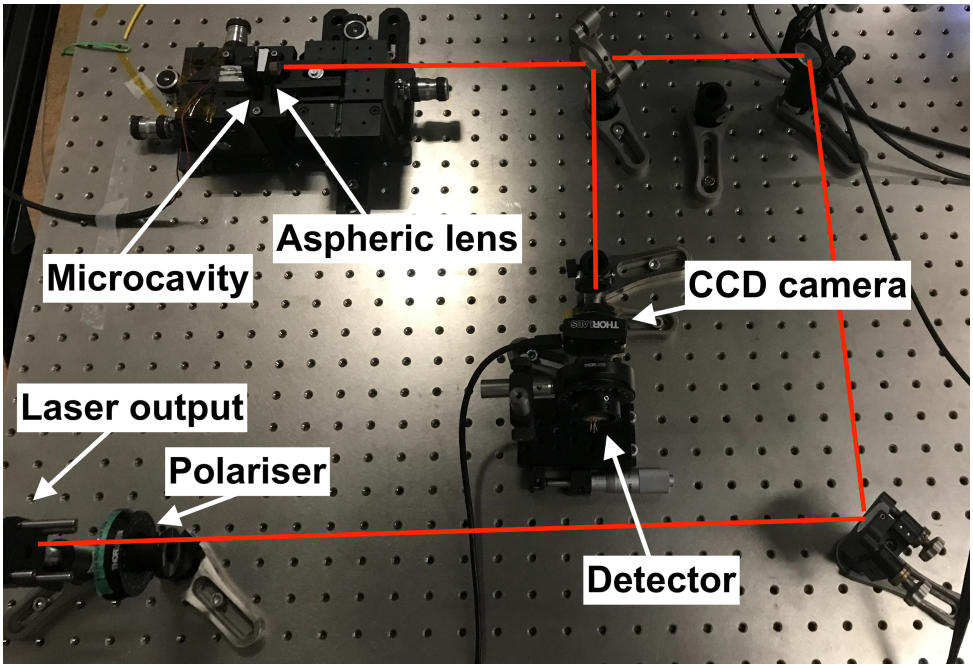

FIGURE 4.6: In this picture the optical setup on the floating table is presented. The laser beam enters the setup in the bottom right corner and is steered into the cavity by the two adjustment mirrors passing the optical components discussed in the text.

Chapter 5

Experimental results

The main goal of this work was to demonstrate an error signal monitoring the length changes of the microcavity. In previous experiments, the group in Lund used side-of-fringe locking to stabilise the microcavity. Tilt locking offers the advantage of locking the cavity directly on the top to the fringe and using a wavelength that sits nm apart from the main resonance wavelength. This chapter demonstrates and discusses experimental results applying the tilt locking scheme on the fibre-based microcavity.

In figure 5.1 a single oscilloscope shot is shown. The displayed signal nicely demonstrates the concept of tilt locking. Comparing it to the theory presented in chapter 2, this is identified as an error signal when the length of the cavity is passing a zeroth-order resonance. Before reaching the resonant length, during negative voltages on the piezo, the left part of the detector is exposed to slightly more power than the right side. This ratio switches after passing the resonant length.

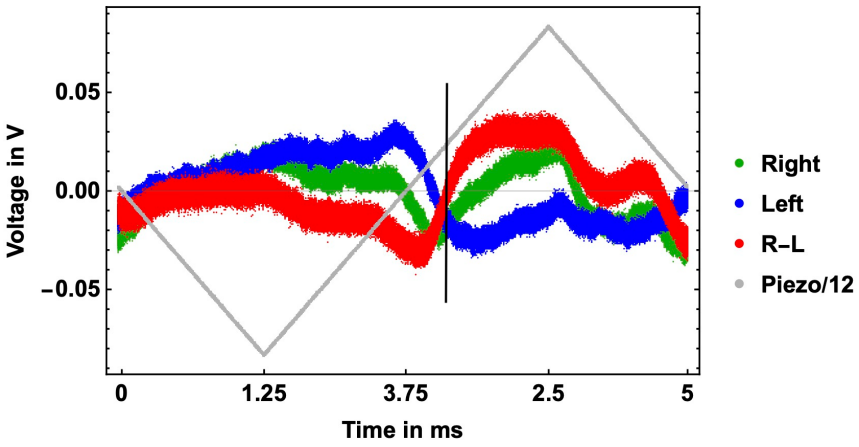

FIGURE 5.1: The blue and the green curves correspond to the light intensity on the two sides of the split-detector, respectively. The error signal in red is given by the subtraction of one side from the other. As the voltage on the piezo increases, the fibre gets pushed forwards, and the cavity becomes resonant with the laser light (indicated by the black bar). In resonance, the light leaking out of the cavity can be detected, and the error signal is formed as explained above.

The resonant length is reached at around the point where the voltages corresponding to the two sides of the detector are equal. At that point, the error signal has its steepest slope. The cavity length passes the resonance again when the voltage on the piezo decreases. The position of the fibre-tip is not precisely linear with the voltage on the piezo because the shear piezo follows a hysteresis curve. This data is taken while applying a 1 V peak to peak voltage amplified by a factor of 25; the frequency is set to 100 Hz. The error signal in this configuration is in the order of a few tens of mV. The size of the error signal is increased below by more than one order of magnitude by adjusting the bias voltage on the detector and better focusing on the active area of the detector.

5.1 Zeroth-order resonance

In figure 5.2 a much stronger error signal is shown; here, the piezo was driven with a 55 Hz and 7 V peak to peak signal before amplification. The cavity length oscillates around a zeroth-order resonance. The cavity is in resonance with the laser around the zero crossings of the piezo driving voltage. The error signal represented in red has a linear steep slope around the resonance. In this plot, the data is averaged over ten samples. This plot shows how the dips of the two sides of the detector are phase-shifted, which is responsible for the error signal here, as discussed in chapter 3.

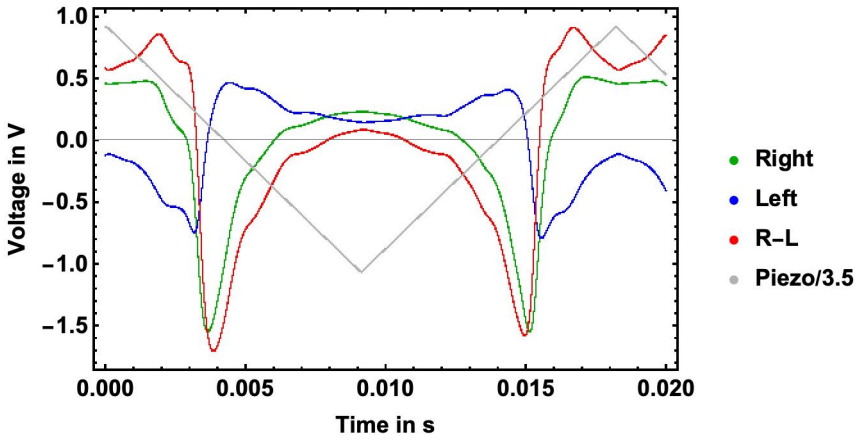

FIGURE 5.2: This plot shows the error signal resulting from the cavity length oscillating around a zeroth-order resonance. The phase shift between the two sides of the split detector can be seen. The resonance is reached when the slope of the error signal is steepest. For high positive voltages on the shear piezo, the cavity is closer to the mirror than the resonance length. Before the first zero crossing of the piezo voltage, the cavity length passes the resonance; at that point, the error function has its steepest slope. After the piezo voltage increases, the length passes the resonance again, and the mirrored error signal occurs.

5.2 First-order resonance

When locking the cavity length to a first-order resonance while the single ion readout is done on the zeroth-order resonance, it enables continuous locking without

disturbing the quantum operations as discussed in chapter 3. Here, it is shown that the error signal around the first-order resonance using tilt locking is comparable to the error signal around the zeroth-order.

When looking at a first-order mode resonance, the polariser is installed in front of the laser to achieve a better signal-to-noise ratio. In the case of a first-order resonance, the power on the two sides of the detector spike in opposite directions after passing the resonant length. This behaviour is shown in figure 5.3. The first resonance of the cavity is roughly when the voltage of the two sides of the detector cross at around 0.002 s. As the voltage on the piezo rises, and the cavity is tuned, resonance occurs again at about 0.008 s. This data set demonstrates that the error signal of the tilt locking technique produces a steep and fairly linear slope around the first-order resonance of the cavity.

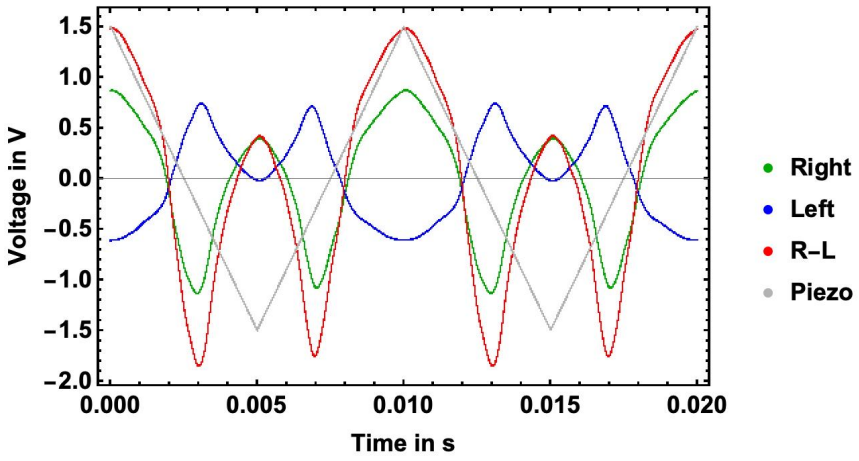

FIGURE 5.3: The blue and the green curves correspond to the power of the two sides of the split-detector, respectively. The error signal is given by the subtraction of the blue one from the green one. As the voltage on the piezo increases, the fibre gets pushed forwards, and the cavity becomes resonant with the used laser light such that the light leaking out of the cavity can be detected, and the error signal can form as described in the text.

5.3 Orientation of the detector

In chapter 4.2 it is discussed that the orientation of the first-order mode needs to be matched with the detector. In figure 5.4 the right picture shows the beam profile of the laser directly attached to the cavity fibre. The cavity is tuned to be resonant in the first-order mode. The left picture shows the beam profile of the light coming from the mirror side without changing the setup. The red circle with a diameter of about 1 mm is drawn in the same position for both pictures clarifying that the two beams overlap on the active area of the camera.

The perfect error signal is achieved when the two intensity maxima of the first-order mode are placed on the two sides of the split detector [31]. This effect is demonstrated in figure 5.5 where one oscilloscope shot is taken when the detector is oriented to match the first-order mode, here called horizontal orientation, and one shot after a 90° rotation called the vertical orientation. The error signal only occurs

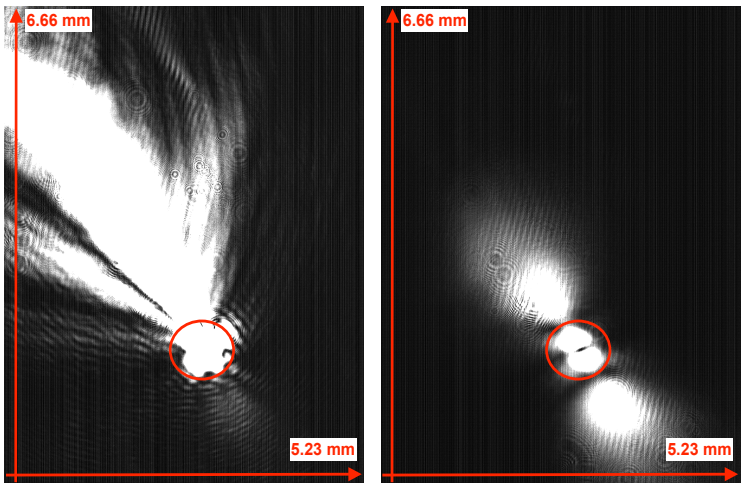

FIGURE 5.4: In both pictures the cavity length is tuned to be resonant with the first order spatial mode. The left picture is taken when the laser is focused from the mirror side onto the cavity. In the right picture, the laser was connected to the fibre forming the cavity. The red circle has a diameter of around 1 mm and is on both pictures in the same position. The blurry effects in both pictures are artifacts from the optical setup. Nevertheless, one can see that the main spot of the reflected laser light is overlapping with the first-order mode of the cavity.

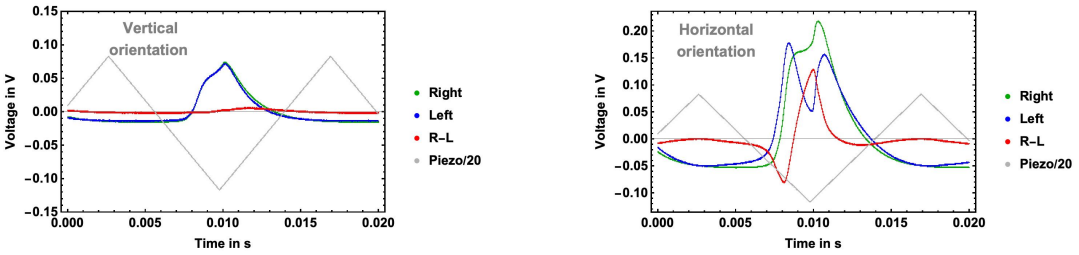

FIGURE 5.5: It is demonstrated that the error signal depends on the detector's rotation. The signal is maximised when the two sides of the detector measure the power of the two maxima of the first-order mode independently. In the left plot, the detector is orientated 90° misaligned to the first-order. In the right-hand figure, the detector is rotated by 90°.

in the horizontal position of the detector because this matches the orientation of the first-order.

5.4 Experimental conclusion

It has been shown that a rather simple setup around the mirror side of the microcavity can return a sufficiently large error signal. The method is able to create a similar error signal both around the first and zeroth-order resonance modes as predicted by the simulations shown in chapter 3. It was demonstrated that higher-order modes could be refocused behind the cavity without cutting off the beam. The collimation was done in a way that is directly implementable into the new microcavity setup.

This error signal could be directly fed back to the piezo to actively stabilise the cavity length.

Chapter 6

Outlook

The new microcavity setup of the quantum information group at Lund's University is currently in the design process. This new design will enable us to optically approach the cavity from the mirror side. In order to focus the laser beam onto the fibre-tip, an aspheric lens is installed before the mirror. Having the opportunity to approach the cavity from the mirror side enables the use of tilt locking.

For the quantum computing experiments with this stabilization, a dedicated laser setup is needed. Here, I discuss what components are needed and available. The tilt locking scheme offers to lock the cavity length independently from the main experiment; the first-order mode of the cavity can be used for locking, while the zeroth order mode is used to read out the Nd ions. The wavelength at which the first order is resonant when the zeroth-order is resonant at 892 nm is displayed in figure 6.1. This resonant wavelength depends on the radius of curvature in the fibre-tip and the length of the microcavity; thus, the laser used for the locking scheme would have to cover a specific wavelength range.

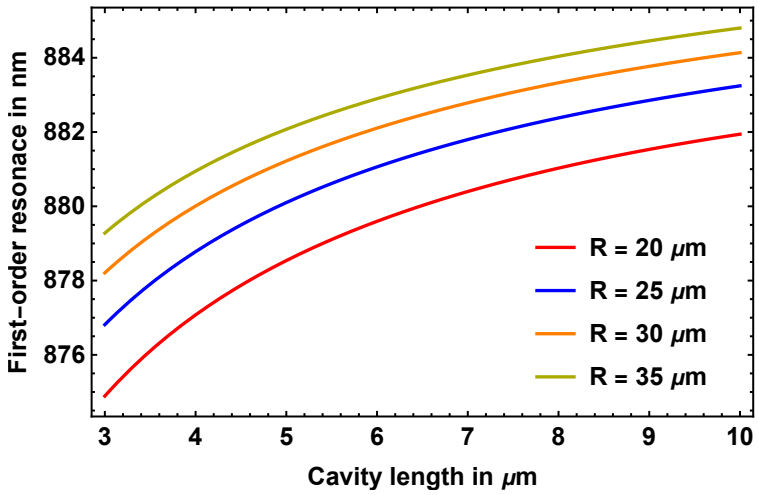

FIGURE 6.1: The first-order mode is resonant at the shown wavelength when the zeroth-order is at a wavelength of 892 nm; the transition wavelength of Neodymium. The resonant wavelength varies depending on the radius of curvature of the fibre-tip and the length of the microcavity.

A dedicated new laser needs to be bought to set up the proposed locking system. The range of the laser would have to be around 875 nm to 885 nm. These kind of tunable lasers are commercially available, for example, from *Sacher Lasertechnik*.

In the setup which will go into the cryostat, the aspheric lens will be fixed to one position. The distance to the fibre-tip will be chosen to collimate the light from the

cavity modes. In order to make the beam match the size of the split detector, another lens between the beam-splitter and the detector is useful. The split detector itself should be placed inside of a rotatable holder. This holder should be mounted on a micrometre stage which covers all three degrees of freedom to find the optimal error signal.

The electric circuit producing a measurable voltage signal from the amperage coming from the detector has a vast potential for improvement. Currently, the voltage is measured across 150 kΩ resistors to amplify the signal, but the noise of a resistor scales with the square root of its resistance. The noise could be reduced by using low noise amplifiers to amplify the signal instead. In the current detector setup, the connections are self-made and have long cables connecting the different parts of the circuit. Long cables pick up electromagnetic signals from the environment; when testing the detector, it was always possible to measure a 50 Hz signal originating in the surrounding electronics. This indicates potential for improvement. There are commercially available products like the *QUAD-4 TRACK* from *Gentec-EO* which are considerably more expansive but solve the electrical setup more professionally and are less sensitive to noise.

The feedback loop of the current locking setup relying on side-of-fringe locking can be reused for tilt locking. The error signal is fed in a *Red Pitaya* which translates the signal into a voltage driving the piezo to readjust the position of the fibre-tip. The error signal of tilt locking can be processed in the same way.

Considering the results given in this thesis, I believe that tilt locking is the best option for building a dedicated locking scheme for microcavities used for single ion interactions. It would enable continuous locking because the wavelength used for locking is nm apart from the main resonance and can be filtered out in the detection setup. Contrary to side-of-fringe locking, it can lock the cavity length on the top of the fringe; and compared to higher order PDH locking, tilt locking promises a stronger error signal while having a lower price-tag.

Appendix A

Overlap integrals

In this appendix, the power transmission into the zeroth, first and second-order microcavity mode, is calculated in detail. The fibre which steers the light towards the cavity is a single-mode fibre; thus, only the zeroth-order transverse mode is transmitted. The beam inside of the fibre can be approximated to have a Gaussian form with a plane wavefront. Knowing the shape of the cavity, the power transmission in the higher-order transverse modes are calculated using the Hermite-Gaussian modes [24]. These are slightly more complicated solutions than the plane wave to the paraxial wave equation, which means they are waves that mainly move in the z-direction. Their wavefront curvature compared to the plane wave is adjusted with an extra factor called the Gouy-shift. This phase shift makes these waves resonant to a slightly different cavity length while having the same wavelength. The general equation for the Hermite–Gaussian modes is:

$$\tilde{u}_n(x,z) = \left(\frac{2}{\pi}\right)^{1/4} \left(\frac{\exp\left[i(2n+1)\Psi(z)\right]}{2^n n! w(z)}\right)^{1/2} H_n\left(\frac{x\sqrt{2}}{w(z)}\right) \exp\left[-i(kz + \frac{kx^2}{2R(z)}) - \frac{x^2}{w^2(z)}\right] \tag{A.1}$$

This is the equation for one transverse dimension, the overall mode can be assembled by multiplying the two transverse dimensions:

$$u_{nm}(x,y,z) = \tilde{u}_n(x,z)\, \tilde{u}_m(y,z) \tag{A.2}$$

Here $w(z)$ is the beam waist of the Gaussian beam which has its minimum at $z = 0$ with $w(z=0) = w_0$ which is called the beam waist. z_0 is the Rayleigh length.

$$\textbf{Rayleigh length: } z_0 = \frac{\pi\omega_0^2}{\lambda} \tag{A.3}$$

$$w(z) = w_0\sqrt{1 + \left(\frac{z}{z_0}\right)^2} \tag{A.4}$$

The radius of curvature is given by:

$$R(z) = z\left[1 + (\frac{z_0}{z})^2\right]. \tag{A.5}$$

The mode matching into the higher orders is calculated with the overlap integral:

$$\left|\int_{-\infty}^{\infty} u(n,x,z,R,L,\lambda)\, u_f^*(x,z,\bar{w},\bar{R},\lambda)dx\right|^2 \tag{A.6}$$

A.1 0. order

The mode in the fibre is similar to a Gaussian shape with a radius of curvature $\bar{R}$ and the beam waist $\bar{w}$ [7].

$$\begin{aligned}
\epsilon_0 &= \frac{2}{\pi}\left|\int_{-\infty}^{\infty}\left(\frac{1}{w}\right)^{1/2}\exp\left[-i\frac{kx^2}{2R}-\frac{x^2}{w^2}\right]\left(\frac{1}{\bar{w}}\right)^{1/2}\exp\left[+i\frac{kx^2}{2\bar{R}}-\frac{x^2}{\bar{w}^2}\right]dx\right|^2 \\
&= \frac{2}{\pi}\frac{1}{w\bar{w}}\left|\int_{-\infty}^{\infty}\exp\left[\left(\frac{ik}{2}\left(\frac{1}{\bar{R}}-\frac{1}{R}\right)-\left(\frac{1}{\bar{w}^2}+\frac{1}{w^2}\right)\right)x^2\right]dx\right|^2 \\
&= \frac{2}{\pi}\frac{1}{w\bar{w}}\left|\frac{\sqrt{\pi}}{\sqrt{\left(\frac{ik}{2}\left(\frac{1}{R}-\frac{1}{\bar{R}}\right)+\left(\frac{1}{\bar{w}^2}+\frac{1}{w^2}\right)\right)}}\right|^2 \\
&= \frac{2}{w\bar{w}\sqrt{\frac{k^2}{4}\left(\frac{1}{R}-\frac{1}{\bar{R}}\right)^2+\left(\frac{1}{\bar{w}^2}+\frac{1}{w^2}\right)^2}} \\
&= \frac{2}{\sqrt{\frac{k^2}{4}w^2\bar{w}^2\left(\frac{1}{R}-\frac{1}{\bar{R}}\right)^2+\frac{\bar{w}^2}{w^2}+\frac{w^2}{\bar{w}^2}+2}} \\
&= \frac{2}{\sqrt{\frac{k^2}{4}w^2\bar{w}^2\left(\frac{1}{R}-\frac{1}{\bar{R}}\right)^2+\left(\frac{\bar{w}}{w}+\frac{w}{\bar{w}}\right)^2}}
\end{aligned}$$

This result matches the result found in [26]. In the case of fibre-tip microcavities, the radius of curvature of the Gaussian beam coming from the fibre is estimated as $\bar{R} = \frac{R_f}{n_f-1}$ where R_f is the radius of curvature of the fibre-tip and n_f is the refractive index of the fibre-core [27]. Following these assumptions, one can rewrite the equation of the power transmission coefficient to:

Power transmission into the 0. Order mode

$$\epsilon_0^2 = \epsilon_{00} = \frac{4}{\left(\frac{\pi(n_f-2)\bar{w}w}{\lambda R}\right)^2+\left(\frac{\bar{w}}{w}+\frac{w}{\bar{w}}\right)^2} \tag{A.7}$$

The beam-waist of the Gaussian beam coming from the fibre $\bar{w}$ can be approximated by the radius of the inner coating of the fibre [27].

A.1.1 Tilted fibre

The fibre can have a slight angle to the mirror indicated in figure 2.6. This angle is a result of thermal contractions or imperfect aligning when glueing the fibre to the mounting stage. This angle would affect the coupling into the higher-order modes enabling a coupling into the odd modes of the cavity. According to [26] the Gaussian beam with a small tilt-angle θ can be expressed as:

$$u_{00}(x,z,\theta) = \left(\frac{2}{\pi w^2}\right)^{1/4}\exp\left[-ikz - i\frac{kx^2}{2R}-\frac{x^2}{w^2}+ik\theta x\right]. \tag{A.8}$$

Following that, the power transmission coefficient in one transverse direction is calculated.

$$\epsilon_0(\theta) = \frac{2}{\pi}\left|\int_{-\infty}^{\infty}\left(\frac{1}{w}\right)^{1/2}\exp\left[-i\frac{kx^2}{2R}-\frac{x^2}{w^2}\right]\times\left(\frac{1}{\bar{w}}\right)^{1/2}\exp\left[+i\frac{kx^2}{2\bar{R}}-\frac{x^2}{\bar{w}^2}+ik\theta x\right]dx\right|^2$$
$$= \frac{2}{\pi}\frac{1}{w\bar{w}}\left|\int_{-\infty}^{\infty}\exp\left[-i\frac{kx^2}{2R}-\frac{x^2}{w^2}\right]\exp\left[+i\frac{kx^2}{2\bar{R}}-\frac{x^2}{\bar{w}^2}+ik\theta x\right]dx\right|^2$$
$$= \frac{2}{\pi}\frac{1}{w\bar{w}}\left|\int_{-\infty}^{\infty}\exp\left[x^2\left(\frac{ik}{2}(\frac{1}{\bar{R}}-\frac{1}{R})-\left(\frac{1}{\bar{w}^2}+\frac{1}{w^2}\right)\right)+ik\theta x\right]dx\right|^2$$

Using the integral:

$$\int_{-\infty}^{\infty}\exp\left[ax^2+bx\right]dx = \sqrt{\frac{\pi}{-a}}\exp\left[-\frac{b^2}{4a}\right]. \tag{A.9}$$

$$\Rightarrow \frac{2}{w\bar{w}}\left|\frac{1}{\sqrt{-\frac{ik}{2}(\frac{1}{\bar{R}}-\frac{1}{R})+(\frac{1}{\bar{w}^2}+\frac{1}{w^2})}}\exp\left[\frac{k^2\theta^2}{4\left(\frac{ik}{2}(\frac{1}{\bar{R}}-\frac{1}{R})-(\frac{1}{\bar{w}^2}+\frac{1}{w^2})\right)}\right]\right|^2$$
$$= \epsilon_0\left|\exp\left[\frac{k^2\theta^2}{4}\left(\frac{1}{\left(\frac{ik}{2}(\frac{1}{\bar{R}}-\frac{1}{R})-(\frac{1}{\bar{w}^2}+\frac{1}{w^2})\right)}\right)\right]\right|^2$$
$$= \epsilon_0\left|\exp\left[\frac{k^2\theta^2}{4}\left(\frac{-\frac{ik}{2}(\frac{1}{\bar{R}}-\frac{1}{R})}{\left(\frac{k^2}{4}(\frac{1}{\bar{R}}-\frac{1}{R})^2+(\frac{1}{\bar{w}^2}+\frac{1}{w^2})^2\right)}+\frac{-(\frac{1}{\bar{w}^2}+\frac{1}{w^2})}{\left(\frac{k^2}{4}(\frac{1}{\bar{R}}-\frac{1}{R})^2+(\frac{1}{\bar{w}^2}+\frac{1}{w^2})^2\right)}\right)\right]\right|^2$$

The complex phase factor disappears in the absolute value.

$$\Rightarrow \epsilon_0\left|\exp\left[\frac{k^2\theta^2}{4}\left(\frac{-(\frac{1}{\bar{w}^2}+\frac{1}{w^2})}{\left(\frac{k^2}{4}(\frac{1}{\bar{R}}-\frac{1}{R})^2+(\frac{1}{\bar{w}^2}+\frac{1}{w^2})^2\right)}\right)\right]\right|^2$$
$$= \epsilon_0\left|\exp\left[-\theta^2\epsilon_0^2\frac{k^2}{16}\left(w^2+\bar{w}^2\right)\right]\right|^2$$
$$= \epsilon_0\exp\left[-\theta^2\epsilon_0^2\frac{k^2}{8}\left(w^2+\bar{w}^2\right)\right]$$

Power transmission into the tilted 0. Order mode

$$\epsilon_{00}(\theta) = \epsilon_{00}\exp\left[-\theta^2\epsilon_{00}\frac{k^2}{8}\left(w^2+\bar{w}^2\right)\right] \tag{A.10}$$

Here the exponential term which is a result of the tilt is not squared because the orientation can always be chosen in such a way that the angle is in one plane. This

matches the results given in [26].

A.2 First-order power transmission coefficient

The overlap into the first-order vanishes if there is no angle between the fibre-tip and the mirror because the odd-numbered Hermite-Gaussian modes are odd functions while the incoming mode is even. If there is a small angle, θ in the alignment of the fibre-tip towards the first-order transverse mode in the cavity is excited.

$$\begin{aligned}\epsilon_1 &= \frac{2}{\pi}\left|\int_{-\infty}^{\infty}\left(\frac{1}{2w}\right)^{1/2}\frac{2\sqrt{2}}{w}x\,\exp\left[-i\frac{kx^2}{2R}-\frac{x^2}{w^2}\right]\times\left(\frac{1}{\bar{w}}\right)^{1/2}\exp\left[+i\frac{kx^2}{2\bar{R}}-\frac{x^2}{\bar{w}^2}+ik\theta x\right]dx\right|^2\\ &= \frac{8}{\pi w^3\bar{w}}\left|\int_{-\infty}^{\infty}x\,\exp\left[x^2\left(\frac{-ik}{2}\left(\frac{1}{R}-\frac{1}{\bar{R}}\right)-\left(\frac{1}{\bar{w}^2}+\frac{1}{w^2}\right)\right)+ik\theta x\right]dx\right|^2\end{aligned}$$

$$\int_{-\infty}^{\infty}x\,\exp\left[(-ia-b)x^2+icx\right]dx=\sqrt{\pi}\frac{ic}{(ia+b)^{(3/2)}}\exp\left[-\frac{c^2}{4(ia+b)}\right]\tag{A.11}$$

$$\begin{aligned}&\Rightarrow\frac{2}{w^3\bar{w}}\left|\frac{ik\theta}{\left(\frac{ik}{2}\left(\frac{1}{R}-\frac{1}{\bar{R}}\right)+\left(\frac{1}{\bar{w}^2}+\frac{1}{w^2}\right)\right)^{3/2}}\exp\left[-\theta^2\epsilon_0^2\frac{k^2}{16}\left(w^2+\bar{w}^2\right)\right]\right|^2\\ &=\frac{2}{w^3\bar{w}}\frac{k^2\theta^2}{\left(\frac{k^2}{4}\left(\frac{1}{R}-\frac{1}{\bar{R}}\right)^2+\left(\frac{1}{\bar{w}^2}+\frac{1}{w^2}\right)^2\right)^{3/2}}\exp\left[-\theta^2\epsilon_0^2\frac{k^2}{8}\left(w^2+\bar{w}^2\right)\right]\\ &=\frac{k^2\theta^2\epsilon_0^3\bar{w}^2}{4}\exp\left[-\theta^2\epsilon_0^2\frac{k^2}{8}\left(w^2+\bar{w}^2\right)\right]\end{aligned}$$

Power transmission into the 1. order mode

$$\epsilon_{10}(\theta)=\frac{k^2\theta^2\epsilon_{00}^2\bar{w}^2}{4}\exp\left[-\theta^2\epsilon_{00}\frac{k^2}{8}\left(w^2+\bar{w}^2\right)\right]\tag{A.12}$$

A.3 Second-order power transmission coefficient

Due to the design of the cavity with one concave and one planar mirror, there will always be an excited second-order transverse mode in the cavity even if the tilt angle is zero.

The second Hermite polynomial is: $H_2(x) = 4x^2 - 2$, thus the power transmission coefficient is calculated as:

$$\epsilon_2(\theta = 0) = \frac{2}{\pi}\left|\int_{-\infty}^{\infty}\left(\frac{1}{8w}\right)^{1/2}\left(\frac{8x^2}{w^2} - 2\right)\exp\left[-i\frac{kx^2}{2R} - \frac{x^2}{w^2}\right] \times \left(\frac{1}{\bar{w}}\right)^{1/2}\exp\left[i\frac{kx^2}{2\bar{R}} - \frac{x^2}{\bar{w}^2}\right]dx\right|^2$$
$$= \frac{1}{\pi w\bar{w}}\left|\int_{-\infty}^{\infty}\left(\frac{4x^2}{w^2} - 1\right)\exp\left[x^2\left(\frac{ik}{2}\left(\frac{1}{\bar{R}} - \frac{1}{R}\right) - \left(\frac{1}{\bar{w}^2} + \frac{1}{w^2}\right)\right)\right]dx\right|^2.$$

Below the solution of the integrals:

$$\int_{-\infty}^{\infty}\exp\left[(ia_i + a_r)x^2\right]dx = \frac{\sqrt{\pi}}{(-ia_i - ar)^{1/2}} \tag{A.13}$$

$$\int_{-\infty}^{\infty}x^2\exp\left[(ia_i + a_r)x^2\right]dx = \frac{\sqrt{\pi}}{2(-ia_i - ar)^{3/2}} \tag{A.14}$$

are used.

$$\Rightarrow \frac{1}{w\bar{w}}\left|\frac{2/w^2}{\left(\frac{ik}{2}\left(\frac{1}{R} - \frac{1}{\bar{R}}\right) + \left(\frac{1}{\bar{w}^2} + \frac{1}{w^2}\right)\right)^{3/2}} - \frac{1}{\left(\frac{ik}{2}\left(\frac{1}{R} - \frac{1}{\bar{R}}\right) + \left(\frac{1}{\bar{w}^2} + \frac{1}{w^2}\right)\right)^{1/2}}\right|^2$$
$$= \frac{1}{w\bar{w}}\left|\frac{2/w^2 - \frac{ik}{2}\left(\frac{1}{R} - \frac{1}{\bar{R}}\right) - \left(\frac{1}{\bar{w}^2} + \frac{1}{w^2}\right)}{\left(\frac{ik}{2}\left(\frac{1}{R} - \frac{1}{\bar{R}}\right) + \left(\frac{1}{\bar{w}^2} + \frac{1}{w^2}\right)\right)^{3/2}}\right|^2$$
$$= \frac{1}{w\bar{w}}\frac{\frac{k^2}{4}\left(\frac{1}{R} - \frac{1}{\bar{R}}\right)^2 + (2/w^2 - \left(\frac{1}{\bar{w}^2} + \frac{1}{w^2}\right))^2}{\left(\frac{k^2}{4}\left(\frac{1}{R} - \frac{1}{\bar{R}}\right)^2 + \left(\frac{1}{\bar{w}^2} + \frac{1}{w^2}\right)^2\right)^{3/2}}$$
$$= \frac{1}{w\bar{w}\left(\frac{k^2}{4}\left(\frac{1}{R} - \frac{1}{\bar{R}}\right)^2 + \left(\frac{1}{\bar{w}^2} + \frac{1}{w^2}\right)^2\right)^{1/2}} - \frac{4}{w^3\bar{w}^3\left(\frac{k^2}{4}\left(\frac{1}{R} - \frac{1}{\bar{R}}\right)^2 + \left(\frac{1}{\bar{w}^2} + \frac{1}{w^2}\right)^2\right)^{3/2}}$$

Power transmission coefficient into the second-order transverse mode

$$\epsilon_{20} = \frac{1}{2}\left(\epsilon_{00} - \epsilon_{00}^2\right) \tag{A.15}$$

A.3.1 Tilted fibre

The second-order is also affected by a tilt of the fibre toward the mirror as calculated below.

$$\epsilon_2(\theta) = \frac{2}{\pi}\left|\int_{-\infty}^{\infty}\left(\frac{1}{8w}\right)^{1/2}\left(\frac{8x^2}{w^2} - 2\right)\exp\left[-i\frac{kx^2}{2R} - \frac{x^2}{w^2}\right] \times \left(\frac{1}{\bar{w}}\right)^{1/2}\exp\left[i\frac{kx^2}{2\bar{R}} - \frac{x^2}{\bar{w}^2} + ik\theta x\right]dx\right|^2$$

$$\begin{aligned}
\epsilon_2(\theta) &= \frac{2}{\pi}\left|\int_{-\infty}^{\infty}\left(\frac{1}{8w\bar{w}}\right)^{1/2}\left(\frac{8x^2}{w^2}-2\right)\exp\left[x^2\left(-i\frac{kx^2}{2}\left(\frac{1}{R}-\frac{1}{\bar{R}}\right)-\left(\frac{1}{\bar{w}^2}+\frac{1}{w^2}\right)\right)+ik\theta x\right]dx\right|^2 \\
&= \frac{1}{\pi w\bar{w}}\left|\int_{-\infty}^{\infty}\left(\frac{4x^2}{w^2}-1\right)\exp\left[x^2\left(-i\frac{kx^2}{2}\left(\frac{1}{R}-\frac{1}{\bar{R}}\right)-\left(\frac{1}{\bar{w}^2}+\frac{1}{w^2}\right)\right)+ik\theta x\right]dx\right|^2 \\
&= \frac{1}{\pi w\bar{w}}\left|\int_{-\infty}^{\infty}\left(\frac{4x^2}{w^2}-1\right)\exp\left[x^2\left(-ia-b\right)+icx\right]dx\right|^2
\end{aligned}$$

Here I substituted for convenience:

$$\begin{aligned}
a &= \frac{k}{2}\left(\frac{1}{R}-\frac{1}{\bar{R}}\right) \\
b &= \frac{1}{w^2}+\frac{1}{\bar{w}^2} \\
c &= k\theta
\end{aligned}$$

Using the solutions of these integrals:

$$\int_{-\infty}^{\infty} dx\, x^2\, \exp\left[(-ia-b)x^2+icx\right] = \sqrt{\pi}\frac{2ia+2b-c^2}{4(ia+b)^{(5/2)}}\exp\left[-\frac{c^2}{4(ia+b)}\right] \tag{A.16}$$

$$\int_{-\infty}^{\infty} dx\, \exp\left[(-ia-b)x^2+icx\right] = \sqrt{\pi}\frac{1}{(ia+b)^{(1/2)}}\exp\left[-\frac{c^2}{4(ia+b)}\right] \tag{A.17}$$

$$= \frac{1}{\pi w \bar{w}} \left| \left(\frac{4\sqrt{\pi}}{w^2} \frac{2ia+2b-c^2}{4(ia+b)^{5/2}} - \frac{\sqrt{\pi}}{(ia+b)^{1/2}} \right) \exp\left[\frac{-c^2}{4(ia+b)} \right] \right|^2$$

$$= \frac{1}{w\bar{w}} \left| \left(\frac{(2ia+2b-c^2)/w^2 - (ia+b)^2}{(ia+b)^{5/2}} \right) \exp\left[\frac{-c^2(-ia+b)}{4\left(a^2+b^2\right)} \right] \right|^2$$

$$= \frac{w^4\bar{w}^4}{32}\epsilon_0^5 \left| \left((2ia+2b-c^2)/w^2 - (ia+b)^2 \right) \right|^2 \exp\left[\frac{-c^2 b}{2\left(a^2+b^2\right)} \right]$$

$$= \frac{w^4\bar{w}^4}{32}\epsilon_0^5 \left| \left(i(\frac{2a}{w^2} - 2ab) + (\frac{2b-c}{w^2} + a^2 - b^2) \right) \right|^2 \exp\left[\frac{-c^2 b}{2\left(a^2+b^2\right)} \right]$$

$$= \frac{w^4\bar{w}^4}{32}\epsilon_0^5 \left(\frac{4a^2}{w^4} - 8\frac{a^2 b}{w^2} + 4a^2b^2 + (\frac{2b-c}{w^2})^2 + a^4 + b^4 + 2a^2\frac{2b-c}{w^2} - 2b^2\frac{2b-c}{w^2} - 2a^2b^2 \right) \times$$
$$\exp\left[\frac{-c^2 b}{2\left(a^2+b^2\right)} \right]$$

$$= \frac{w^4\bar{w}^4}{32}\epsilon_0^5 \left(a^4 + b^4 + 2a^2b^2 - 4\frac{a^2 b}{w^2} - 4\frac{b^3}{w^2} + \frac{4a^2}{w^4} + \frac{4b^2}{w^4} - \frac{4bc}{w^4} + \frac{c^2}{w^4} - 2a^2\frac{c}{w^2} + 2b^2\frac{c}{w^2} \right) \times$$
$$\exp\left[\frac{-c^2 b}{2\left(a^2+b^2\right)} \right]$$

$$= \frac{w^4\bar{w}^4}{32}\epsilon_0^5 \left(\left(a^2+b^2\right)^2 - \frac{4b}{w^2}\left(a^2+b^2\right) + \frac{4}{w^4}\left(a^2+b^2\right) + \frac{c}{w^2}\left(\frac{c}{w^2} - \frac{4b}{w^2} + 2\left(-a^2+b^2\right) \right) \right) \times$$
$$\exp\left[\frac{-c^2 b}{2\left(a^2+b^2\right)} \right]$$

Knowing that:

$$\left(a^2+b^2\right)^2 = \frac{16}{w^4\bar{w}^4\epsilon_0^4}$$
$$\left(a^2+b^2\right) = \frac{4}{w^2\bar{w}^2\epsilon_0^2}$$

the solution is written as shown below.

Power transmission coefficient into the tilted second-order transverse mode

$$\epsilon_{20}(\theta) = \left(\frac{1}{2}\epsilon_{00} - \frac{1}{2}\epsilon_{00}^2 + \Xi(\theta)\epsilon_{00}^3 \right) \exp\left[-\theta^2 \left(\frac{k^2}{8}\epsilon_{00}(w^2+\bar{w}^2) \right) \right] \tag{A.18}$$

$$\approx \frac{1}{2}\left(\epsilon_{00} - \epsilon_{00}^2\right) \exp\left[-\theta^2\epsilon_{00}\frac{k^2}{8}\left(w^2+\bar{w}^2\right) \right] \tag{A.19}$$

Where:

$$\Xi(\theta) = k\theta\frac{\bar{w}^4}{32}\left(k\theta - 4\left(\frac{1}{w^2} + \frac{1}{\bar{w}^2} \right) + 2w^2\left(\left(\frac{1}{w^2} + \frac{1}{\bar{w}^2} \right)^2 - \frac{k^2}{4}\left(\frac{1}{R} - \frac{1}{\bar{R}} \right)^2 \right) \right) \tag{A.20}$$

The ϵ_{00}^3 term is neglectable because $\Xi(\theta) \ll \frac{1}{2}\left(\epsilon_{00} - \epsilon_{00}^2\right)$.

Appendix B

Optical properties of the cavity

B.1 Derivation of a standing wave inside a cavity

To be a mode of the cavity, the beam has to have the same properties after one round trip. The whole information about a Gaussian beam is in its q value:

$$q(z) = z + iz_0 \tag{B.1}$$

where $z_0 = \frac{\pi\omega_0^2}{\lambda}$ is the Rayleigh length and $\frac{1}{q(z)} = \frac{1}{R(z)} - i\frac{\lambda}{\pi\omega^2(z)}$. Here the matrix method is used to find the properties of the Gaussian mode which is an eigen-mode of the cavity [23].

$$\begin{bmatrix} 1 & l \\ 0 & 1 \end{bmatrix} \begin{bmatrix} 1 & 0 \\ -2/R & 1 \end{bmatrix} \begin{bmatrix} 1 & l \\ 0 & 1 \end{bmatrix} = \begin{bmatrix} 1 - \frac{2l}{R} & 2l - \frac{2l^2}{R} \\ -2/R & 1 - \frac{2l}{R} \end{bmatrix} \tag{B.2}$$

The formula to transform from q_1 through an optical apparatus to a q_2 is used. In this case for the stable mode it needs to meet the condition $q_1 = q_2$.

$$q_2 = \frac{Aq_1 + B}{Cq_1 + D} \tag{B.3}$$

$$0 = \frac{B}{q^2} + \frac{(A - D)}{q} - C \tag{B.4}$$

$$\frac{1}{q} = \frac{-(A - D)}{2B} \pm \frac{\sqrt{(A - D)^2 + 4BC}}{2B} \tag{B.5}$$

The stability requirements are defined.

$$AD - BC = 1 \tag{B.6}$$

$$4BC = 4AD - 4 \tag{B.7}$$

$$A + D/2 - 1 \leq 1 \tag{B.8}$$

Thus the equation is simplified.

$$\frac{1}{q} = \frac{(D - A)}{2B} \pm i\frac{\sqrt{1 - \left(\frac{A+D}{2}\right)^2}}{B} \tag{B.9}$$

The Beam-waist is at $z = 0$ which corresponds to the surface of the flat mirror.

$$\omega_0 = \left(\frac{\lambda}{\pi}\right)^{1/2} \sqrt{\frac{B}{\sqrt{1-\left(\frac{A+D}{2}\right)^2}}} \tag{B.10}$$

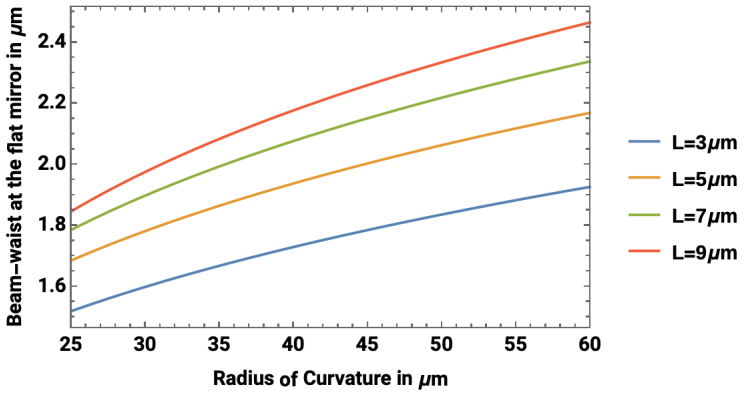

FIGURE B.1: The beam-waist ω_0 at the flat mirror is fully confined by the properties of the cavity. This plot shows the calculated beam-waist for typical values in the microcavity for a wavelength of $\lambda = 890nm$. The beam-waist is plotted for different length L of the micro-cavity.

B.2 Calculating the beam going out of the mirror

The matrix for a plane surface with two refractive index n_1 and n_2 is given by:

$$\begin{bmatrix} 1 & 0 \\ 0 & n_1/n_2 \end{bmatrix} \tag{B.11}$$

this is used to calculate the q_2 after the surface.

$$q_2 = i\frac{z_0 n_2}{n_1} \tag{B.12}$$

The part of the pass that travelled through the mirror with the different refractive index is taken into account.

$$q_3 = i\frac{z_0 n_2}{n_1} + d_{mirror} \tag{B.13}$$

Before leaving the mirror on the other side it passes the outer surface of the mirror.

$$q_4 = iz_0 + d_{mirror}\frac{n_1}{n_2} \tag{B.14}$$

The expansion of the beam waist must be known to choose the right lens to collimate the light without losing the transverse shape of the higher orders. The calculated beam-waist is shown in figure B.2 and B.3. The lens in the setup needs to have a large enough diameter. This diameter of the clear apparatus must be at least twice the beam waist dependent on the distance from the inner plane of the flat mirror.

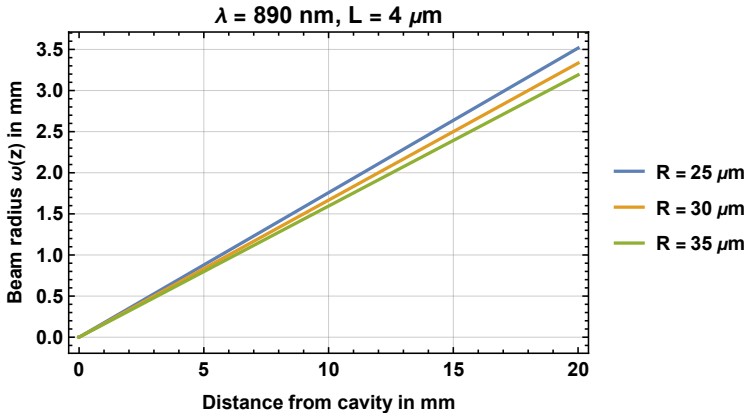

FIGURE B.2: The radius of the beam $\omega(z)$ growing over distance from the cavity. For a cavity with length of 4 µm and different radii of curvature.

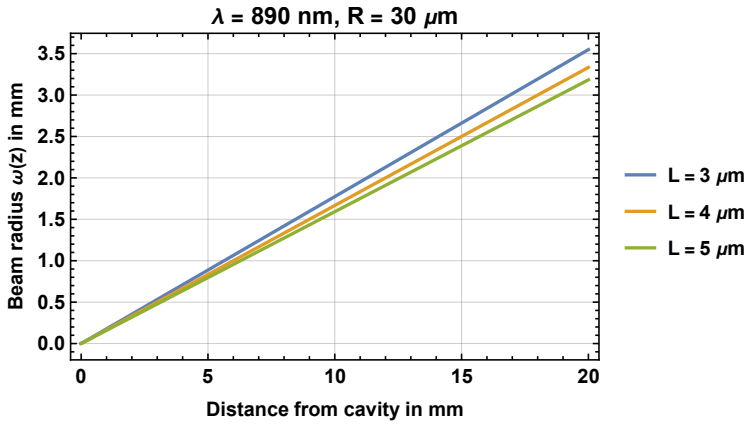

FIGURE B.3: The radius of the beam $\omega(z)$ growing over distance from the cavity. For a cavity with a radius of curvature of 30 µm and different cavity lengths.

Bibliography

[1] Adam Kinos et al. *Roadmap for Rare-earth Quantum Computing*. 2021. arXiv: 2103.15743 [quant-ph].

[2] Richard P. Feynman. "Simulating physics with computers". In: *Int.J.Theor.Phys.* 21 (June 1982), pp. 467–488. DOI: https://doi.org/10.1007/BF02650179.

[3] Frank Arute et al. "Quantum supremacy using a programmable superconducting processor". In: *Nature* 574 (Oct. 2019), pp. 505–510. DOI: 10.1038/s41586-019-1666-5.

[4] Han-Sen Zhong et al. "Quantum computational advantage using photons". In: *Science* 370.6523 (2020), pp. 1460–1463. ISSN: 0036-8075. DOI: 10.1126/science.abe8770. eprint: https://science.sciencemag.org/content/370/6523/1460.full.pdf. URL: https://science.sciencemag.org/content/370/6523/1460.

[5] A. Walther et al. "High-fidelity readout scheme for rare-earth solid-state quantum computing". In: *Physical Review A* 92 (Aug. 2015). DOI: 10.1103/PhysRevA.92.022319.

[6] E. M. Purcell. "Proceedings of the American Physical Society". In: *Physical Review* 69.11-12 (June 1946), pp. 674–674. DOI: 10.1103/PhysRev.69.674.

[7] T. Steinmetz et al. "Stable fiber-based Fabry-Pérot cavity". In: *Applied Physics Letters* 89 (Oct. 2006), pp. 111110 –111110. DOI: 10.1063/1.2347892.

[8] Eric Black. "An introduction to Poun-Drever-Hall laser frequency stabilization". In: *American Journal of Physics* 69 (Jan. 2001), pp. 79–87. DOI: 10.1119/1.1286663.

[9] Bram Slagmolen et al. "Frequency stability of spatial mode interference (tilt) locking". In: *Quantum Electronics, IEEE Journal of* 38 (Dec. 2002), pp. 1521 – 1528. DOI: 10.1109/JQE.2002.804267.

[10] B. P. Abbott et al. "Observation of Gravitational Waves from a Binary Black Hole Merger". In: *Phys. Rev. Lett.* 116 (6 Feb. 2016), p. 061102. DOI: 10.1103/PhysRevLett.116.061102. URL: https://link.aps.org/doi/10.1103/PhysRevLett.116.061102.

[11] Adam Kinos. "Light-Matter Interaction and Quantum Computing in Rare-Earth-Ion-Doped Crystals". PhD thesis. Lund University, Feb. 2018. ISBN: 978-91-7753-543-0.

[12] Michael A. Nielsen and Isaac L. Chung. *Quantum Computation and Quantum Information*. Cambridge: Cambridge University Press, 2010. ISBN: 978-1-107-00217-3. URL: www.cambridge.org/9781107002173.

[13] David DiVincenzo and IBM. "The Physical Implementation of Quantum Computation". In: *Fortschritte der Physik* 48 (Mar. 2000). DOI: 10.1002/1521-3978(200009)48:9/11<771::AID-PROP771>3.0.CO;2-E.

[14] M Devoret and R Schoelkopf. "Superconducting Circuits for Quantum Information: An Outlook". In: *Science (New York, N.Y.)* 339 (Mar. 2013), pp. 1169–74. DOI: 10.1126/science.1231930.

[15] Henning Hahn et al. "Integrated 9Be+ multi-qubit gate device for the ion-trap quantum computer". In: *npj Quantum Information* 5 (Dec. 2019). DOI: 10.1038/s41534-019-0184-5.

[16] Jonathan P. Home et al. "Complete Methods Set for Scalable Ion Trap Quantum Information Processing". In: *Science* 325.5945 (2009), pp. 1227–1230. ISSN: 0036-8075. DOI: 10.1126/science.1177077. eprint: https://science.sciencemag.org/content/325/5945/1227.full.pdf. URL: https://science.sciencemag.org/content/325/5945/1227.

[17] A. J. Freeman and R. E. Watson. "Theoretical Investigation of Some Magnetic and Spectroscopic Properties of Rare-Earth Ions". In: *Phys. Rev.* 127 (6 Sept. 1962), pp. 2058–2075. DOI: 10.1103/PhysRev.127.2058. URL: https://link.aps.org/doi/10.1103/PhysRev.127.2058.

[18] Andreas Walther. "Coherent Processes in Rare-Earth-Ion-Doped Solids". PhD thesis. Atomic Physics, 2009. ISBN: 978-91-628-7718-7.

[19] Mouktik Raha et al. "Optical quantum nondemolition measurement of a single rare earth ion qubit". In: *Nature Communications* 11 (Mar. 2020). DOI: 10.1038/s41467-020-15138-7.

[20] R Kolesov et al. "Optical detection of a single rare-earth ion in a crystal". In: *Nature communications* 3 (Aug. 2012), p. 1029. DOI: 10.1038/ncomms2034.

[21] Andreas Reiserer and Gerhard Rempe. "Cavity-based quantum networks with single atoms and optical photons". In: *Rev. Mod. Phys.* 87 (4 Dec. 2015), pp. 1379–1418. DOI: 10.1103/RevModPhys.87.1379. URL: https://link.aps.org/doi/10.1103/RevModPhys.87.1379.

[22] Michael Harvey and Andrew White. "Frequency Locking by Analysis of Orthogonal Modes". In: *Optics Communications* 221 (June 2003). DOI: 10.1016/S0030-4018(03)01425-1.

[23] Bahaa E A Saleh and Malvin Carl Teich. *Fundamentals of photonics; 2nd ed.* Wiley series in pure and applied optics. New York, NY: Wiley, 2007. URL: https://cds.cern.ch/record/1084451.

[24] A.E. Siegman. *Lasers*. University Science Books, 1986. ISBN: 9780935702118. URL: https://books.google.se/books?id=1BZVwUZLTkAC.

[25] Simin Feng and Herbert G. Winful. "Physical origin of the Gouy phase shift". In: *Opt. Lett.* 26.8 (Apr. 2001), pp. 485–487. DOI: 10.1364/OL.26.000485. URL: http://ol.osa.org/abstract.cfm?URI=ol-26-8-485.

[26] W. B. Joyce and B. C. DeLoach. "Alignment of Gaussian beams". In: *Appl. Opt.* 23.23 (Dec. 1984), pp. 4187–4196. DOI: 10.1364/AO.23.004187. URL: http://ao.osa.org/abstract.cfm?URI=ao-23-23-4187.

[27] D Hunger et al. "A fiber Fabry–Perot cavity with high finesse". In: *New Journal of Physics* 12.6 (June 2010), p. 065038. DOI: 10.1088/1367-2630/12/6/065038. URL: https://doi.org/10.1088%2F1367-2630%2F12%2F6%2F065038.

[28] Julia Maria Helene Benedikter. "Microcavity Enhancement of Silicon Vacancy Centres in Diamond and Europium Ions in Yttria". PhD thesis. Ludwig Maximilian Universität München, 2019.

[29] Brian M. Walsh et al. "Spectroscopic characterization of Nd:Y2O3: application toward a differential absorption lidar system for remote sensing of ozone". In: *J. Opt. Soc. Am. B* 19.12 (Dec. 2002), pp. 2893–2903. DOI: 10.1364/JOSAB.19.002893. URL: http://josab.osa.org/abstract.cfm?URI=josab-19-12-2893.

[30] R. W. P. Drever et al. "Laser phase and frequency stabilization using an optical resonator". In: *Applied Physics B* 97 (June 1983), pp. 1432–0649. DOI: 10.1007/BF00702605.

[31] Yan You et al. "High finesse pulsed optical cavity locking by tilt-locking technique". In: *Review of Scientific Instruments* 85 (Mar. 2014), pp. 033102–033102. DOI: 10.1063/1.4867247.

[32] Yves Colombe et al. "Strong atom-field coupling for Bose-Einstein condensates in an optical cavity on a chip". In: *Nature* 450 (Dec. 2007), pp. 272–6. DOI: 10.1038/nature06331.